

Geological Society, London, Special Publications

## Mapping volcanic terrain using high-resolution and 3D satellite remote sensing

M. Kervyn, F. Kervyn, R. Goossens, S. K. Rowland and G. G. J. Ernst

*Geological Society, London, Special Publications* 2007; v. 283; p. 5-30  
doi:10.1144/SP283.2

---

### Email alerting service

[click here](#) to receive free email alerts when new articles cite this article

### Permission request

[click here](#) to seek permission to re-use all or part of this article

### Subscribe

[click here](#) to subscribe to Geological Society, London, Special Publications or the Lyell Collection

---

### Notes

**Downloaded by**      on 14 November 2007

---

# Mapping volcanic terrain using high-resolution and 3D satellite remote sensing

M. KERVYN<sup>1</sup>, F. KERVYN<sup>2</sup>, R. GOOSSENS<sup>3</sup>, S. K. ROWLAND<sup>4</sup> & G. G. J. ERNST<sup>1</sup>

<sup>1</sup>*Mercator & Ortelius Research Centre for Eruption Dynamics, Department of Geology and Soil Sciences, Ghent University, Krijgslaan 281/S8, B-9000 Gent, Belgium (e-mail: Matthieu.KervynDeMeerendre@UGent.be)*

<sup>2</sup>*Cartography & Photo-Interpretation Section, Geology and Mineralogy Department, Royal Museum for Central Africa, Leuvensesteenweg 13, B-3080 Tervuren, Belgium*

<sup>3</sup>*Remote Sensing & Photogrammetry, Department of Geography, Ghent University, Krijgslaan 281/S8, B-9000 Gent, Belgium*

<sup>4</sup>*Department of Geology & Geophysics, University of Hawai'i at Mānoa, 1680 East–West Road, Honolulu, HI 96822, USA*

**Abstract:** Most of the hazardous volcanoes, especially those in developing countries, have not been studied or regularly monitored. Moderate-to-high spatial resolution and 3D satellite remote sensing offers a low-cost route to mapping and assessing hazards at volcanoes worldwide. The capabilities of remote sensing techniques are reviewed and an update of recent developments is provided, with emphasis on low-cost data, including optical (Landsat, ASTER, SPOT, CORONA), topographic (3D ASTER, SRTM) and synthetic aperture radar data. Applications developed here illustrate capabilities of relevant remote sensing data to map hazardous volcanic terrain and derive quantitative data, focusing on mapping and monitoring of volcanic morphology. Limitations of the methods, assessment of errors and planned new sensors are also discussed.

The volcanology community has long recognized the advantages of multispectral and synthetic aperture radar (SAR) remote sensing (RS) techniques. The multispectral nature of the data and the repeated coverage of extensive volcanic terrains are major advantages. For over two decades, satellite data have been used to study volcanic activity and map volcanic terrains (e.g. Francis & Baker 1978; Mougini-Mark *et al.* 2000; Ramsey & Dean 2004; Ramsey & Flynn 2004). Spaceborne sensors permit observation of volcanoes that are remote or difficult to access for political reasons. Sensors allow information retrieval from ongoing eruptive activity for which field data collection is too hazardous. Satellite data allow study of diverse volcanic phenomena (e.g. Francis *et al.* 1996), including to:

- (1) detect hot areas, their temporal and spatial patterns (e.g. Harris *et al.* 2000);
- (2) monitor volcanic clouds (e.g. Rose *et al.* 2000);
- (3) map recently erupted volcanic (e.g. Patrick *et al.* 2003; Rowland *et al.* 2003) or volcano-related deposits (e.g. lahars, debris avalanches; Kerle *et al.* 2003);
- (4) discriminate fresh volcanic rock surfaces in terms of mineralogical, textural and compositional

differences (e.g. Gaddis 1992; Ramsey & Fink 1999; Byrnes *et al.* 2004);

- (5) distinguish weathered volcanic surfaces and assess the terrains' relative age (e.g. Kahle *et al.* 1988), or identify mechanically weak sectors in a volcanic edifice (Crowley & Zimelman 1997);

- (6) characterize volcano morphology and study its changes (e.g. Amelung *et al.* 2000; Rowland & Garbeil 2000; Lu *et al.* 2003);

- (7) assess ground deformation using interferometric synthetic aperture radar (InSAR; e.g. Zebker *et al.* 2000).

The potential of high temporal resolution satellite imagery for monitoring volcanic activity and mitigating hazards has been reviewed by Oppenheimer (1998) and Harris *et al.* (2000). Thanks to increased RS data accessibility and reduced time between data acquisition and availability to users (Ramsey & Flynn 2004), low-to-medium spatial resolution (>1 km to 250 m pixel) satellite data are now routinely used to monitor volcanoes; for example, to detect thermal anomalies (Wright *et al.* 2004), or to detect and track ash- and gas-rich volcanic clouds (e.g. Rose *et al.* 2000; Ramsey & Dean 2004). It is not the purpose of this paper to review RS capabilities to monitor

eruptive events (for that, see Mouginiis-Mark *et al.* 2000), but instead to focus on assessing future hazards by mapping the distribution of existing eruption-related features.

Until recently, research focused on monitoring active volcanoes or on studying *a posteriori* volcanic events and their deposits. Repose periods between eruptions can be decades to thousands of years long. Some of the largest and most devastating historical eruptions occurred at volcanoes that had been considered as dormant or inactive (e.g. 1991 Mt Pinatubo; Newhall & Punongbayan 1996). The majority of the *c.* 560 on-land historically active volcanoes are poorly known (Simkin & Siebert 1994). Fewer than a quarter of them have detailed hazards maps, and fewer still are regularly monitored. Many of these potentially hazardous volcanoes are located in developing countries, where local systems struggle to assess and mitigate volcanic hazards.

For hazard assessment and risk modelling, there is an obvious need to map and characterize the range of deposit types at poorly known or remote volcanoes, to infer the range of activity that they might exhibit. Prior to geological mapping, one needs a good topographic map, also essential for modelling volcanic processes and risks, such as pyroclastic, lava and mud flows (e.g. Iverson *et al.* 1998; Stevens *et al.* 2002; Sheridan *et al.* 2004). Sources of spatial data, such as aerial photography and good quality topographic maps (e.g. 1:25 000 or better), either do not exist or are very difficult to obtain for many volcanically active regions. The goal of this paper is to illustrate how medium-to-high spatial resolution (*c.* 10 to 100 m pixel) satellite imagery provided by multispectral (e.g. Landsat, ASTER, SPOT, CORONA) and SAR sensors (e.g. ERS-1, ERS-2, SRTM) is helpful both for deriving accurate topographic and geological maps and for assessing volcanic hazards.

A key development is that the availability of medium-resolution (*c.* 30 m pixel) satellite images over the Internet has increased dramatically, together with a rapid decrease in cost (Table 1). Satellite RS techniques (InSAR, digital stereo-photogrammetry) now provide some of the best digital topographic datasets. These improvements will help the systematic assessment of geohazards at poorly studied volcanoes. However, there is a need to assess the accuracy of the quantitative data retrieved from satellite imagery.

In this paper, we assess the capabilities of satellite data to map and quantitatively study the structure, morphology and texture of volcanic terrains at different scales, to gain insights into processes and assess hazards. We review previous studies, provide an update on advances and present new

case studies to illustrate satellite data use for mapping volcanoes. We review the ability of multi-spectral and SAR sensors to map volcanic deposits, as well as InSAR's capability to generate digital elevation data, aiding morphological studies. A first case study illustrates the potential of ASTER and CORONA data to provide high-resolution and up-to-date topographic maps. The approach, illustrated for a non-volcanic region of Morocco, can be readily applied to volcanic regions. The second case study (Mauna Kea, Hawai'i) illustrates use of multispectral imagery and SRTM DEM data to map small-scale volcanic features. The goal is to examine the advantages and limitations of RS data types available for developing countries, using a volcanic test area where data cross-validation allows accuracy assessments. With the third case study, we then explore to what extent the RS data can be used for the rapid mapping of geohazards and terrain types, including the monitoring of ground deformation, at the Rungwe Volcanic Province (RVP), SW Tanzania. Finally, we highlight some future perspectives for systematic risk assessment at volcanoes, especially in less developed countries, through integrated RS studies and through the increased capabilities that planned new sensors will provide.

## Multispectral and digital elevation model data

An ever-increasing number of spaceborne sensors continue to provide a wealth of high-quality multispectral data. This study focuses on the moderate-to-high spatial resolution (*c.* 10 to 100 m pixel) sensors needed to study volcanoes and that are easily accessible at low cost (Table 1). Very high spatial resolution (*c.* 1 m pixel) data provided by commercial sensors (e.g. Ikonos, Quickbird) are not yet a low-cost alternative to assess volcanic hazards (Table 1), even though such sensors prove helpful to produce up-to-date orthomaps for some active volcanoes (e.g. Nisyros caldera, Greece; Vassilopoulou *et al.* 2002). Airborne RS, although very useful, is not discussed here because it is comparatively expensive, with coverage restricted to relatively few volcanoes.

Multispectral images are a record of reflected or emitted electromagnetic energy. The data range from visible (VIS), near-infrared (NIR), and mid-infrared (MIR) wavelengths (solar energy reflected by the surface) to thermal-infrared (TIR; solar energy absorbed and then re-emitted by the surface). Multispectral data are considered here from Landsat, SPOT, ASTER and CORONA sensors (properties summarized in Table 1). Digital Elevation Model's (DEM) of volcanic terrains

**Table 1.** Characteristics and sources of RS data discussed in the text

Sensor	Number of bands and spatial resolution	Scene size	Cost	Data distributor	Distributor website
<i>Medium- to high-resolution optical sensors</i>					
Landsat ETM+	PAN: 1 band 15 m VNIR + SWIR: 6 bands 30 m	180 × 180 km <sup>2</sup>	Free	Global Land Cover Facility, University of Maryland	<a href="http://glcfapp.umiacs.umd.edu/index.shtml">http://glcfapp.umiacs.umd.edu/index.shtml</a>
ASTER	TIR: 1 band 60 m VNIR: 3 bands 15 m SWIR: 6 bands 30 m TIR: 5 bands 90 m	61.5 × 63 km <sup>2</sup>	Free	Land Processes Distributed Active Archive Center (LPDAAC)	<a href="http://edcdaac.usgs.gov/datapool/datapool.asp">http://edcdaac.usgs.gov/datapool/datapool.asp</a>
			US\$ 55	NASA Earth Observing System Data Gateway	<a href="http://redhook.gsfc.nasa.gov/~imswww/pub/imswelcome/">http://redhook.gsfc.nasa.gov/~imswww/pub/imswelcome/</a>
			Free	Global Land Cover Facility, University of Maryland	<a href="http://glcfapp.umiacs.umd.edu/index.shtml">http://glcfapp.umiacs.umd.edu/index.shtml</a>
SPOT 5	PAN: 1 band 5 m VNIR: 3 bands 10 m SWIR: 1 band 20 m	60 × 60 km <sup>2</sup>	€100–800* €1200–6200	Spotimage	<a href="http://www.spotimage.fr">www.spotimage.fr</a>
CORONA	PAN: 2–30 ft (c. 0.6–9 m)	c. 14 × 200 km <sup>2</sup> (KH 1–4)	US\$ 24–45	USGS Earth Explorer	<a href="http://edcsns17.cr.usgs.gov/EarthExplorer/">http://edcsns17.cr.usgs.gov/EarthExplorer/</a>
<i>Very high-resolution optical sensors</i>					
IKONOS	PAN: 1 band 1 m VNIR: 4 bands 4 m	>49 km <sup>2</sup> 11 km swath width	US\$ 7–56 km <sup>-2</sup>	Space Imaging	<a href="http://www.spaceimaging.com">www.spaceimaging.com</a>
Quickbird	PAN: 1 band 0.6 m VNIR: 4 bands 2.4 m	>25 km <sup>2</sup> 16.5 km swath width	€18–42 km <sup>-2</sup>	DigitalGlobe	<a href="http://www.digitalglobe.com">www.digitalglobe.com</a>
<i>Synthetic aperture radar</i>					
ERS-1 &-2	C-band 25 m	100 × 110 km <sup>2</sup>	€400–1400	Eurimage	<a href="http://www.eurimage.com">www.eurimage.com</a>
RADARSAT	C-band 30 m	100 × 100 km <sup>2</sup>	US\$2750–4250	Radarsat International	<a href="http://www.rsi.ca">www.rsi.ca</a>
JERS SAR	L-band 18 m	75 × 75 km <sup>2</sup>	€950	Eurimage	<a href="http://www.eurimage.com">www.eurimage.com</a>
<i>Digital elevation models</i>					
SRTM C-band	C-band: 30 m	1° lat–long	Free; US only	Seamless Data Distribution System	<a href="http://seamless.usgs.gov">http://seamless.usgs.gov</a>
	C-band: 90 m	1° lat–long	Free	Seamless Data Distribution System	<a href="http://seamless.usgs.gov">http://seamless.usgs.gov</a>
SRTM X-band	X-band: 25 m	0.25° lat–long	€400	EOWEB, German Aerospace Agency	<a href="http://www.eoweb.dlr.de">www.eoweb.dlr.de</a>
SPOT HRS	PAN: 10 m	>3000 km <sup>2</sup> ; 120 km swath width	€2.3 km <sup>-2</sup>	Spotimage	<a href="http://www.spotimage.fr">www.spotimage.fr</a>

\*Only for European scientific users.

Range of price is indicative, varying with processing level, data type (archived or newly acquired data), and delivery time. Data distributors are given as examples of where those data can be acquired.

can be obtained by: (i) digital photogrammetry based on stereoscopic pair of aircraft of satellite images; (ii) digitalization and interpolation of topographic maps; (iii) radar interferometry; (iv) laser scanning or (v) field survey. Advantages and limitations of the different DEM-generation techniques have been received by Baldi *et al.* (2002) and Stevens *et al.* (e.g. 2002, 2004).

### *Landsat*

The Enhanced Thematic Mapper + (ETM+) instrument onboard the Landsat 7 satellite acquires data in six bands at VIS to MIR wavelengths at 30 m spatial resolution. It also provides a panchromatic band (i.e. black and white) spanning the visible spectrum at 15 m spatial resolution, and two TIR bands (at the same wavelength but with different gain settings) at 60 m spatial resolution (Williams 2003). An ETM+ scene ( $180 \times 180 \text{ km}^2$ ) covers a much larger area than that of an airphoto; it does not suffer from radial distortion (after systematic data pre-processing), and it is cheaper than airphoto coverage for the same area. The ETM+ image discussed here was downloaded, for free, from the Global Land Cover Facilities website (GLCF 2005; Table 1). Similar archive images are now freely available for most regions. The Landsat generation of satellites has acquired data since 1972, resulting in a large volume of available archived data. On request, a new image can be acquired, over any given region, every 16 days. However, the cost of on-request data remains high (up to €600; Eurimage website 2005). Regions for which no specific data acquisition requests have been made might not be covered by cloud-free data for several years.

Data acquired by the Thematic Mapper (TM) and ETM+ instruments onboard the Landsat 5 and 7 satellites, respectively, have been used to monitor volcanic activity as these were the first sensors to provide sufficiently fine spatial resolution to map the extent, and characterize the spatial evolution, of hot volcanic areas (e.g. lava flows or domes; e.g. Harris *et al.* 2004). The fine spatial resolution of TM data was also exploited to identify potentially active volcanoes in the Andes (Francis & De Silva 1989) based on crater morphology, lava flow texture and evidence of post-glacial eruptive activity. TM's spectral capability also proved useful for identifying and mapping the distribution of distinct lithologies within volcanic debris avalanches (e.g. Francis & Wells 1988; Wadge *et al.* 1995), and for identifying basaltic scoria cones with specific iron oxidation features in dry environments (e.g. Chagarlamudi & Moufti 1991). Landsat data are now often used in morphological studies of volcanoes or *a posteriori* descriptions of a volcanic

event because they easily provide a synoptic view of a volcano across multiple wavelengths (e.g. Patrick *et al.* 2003). On the other hand, the temporal resolution (16 days at best), time lag between image acquisition and availability to users (1–14 days), and high cost of on-request data over specific targets prevent true real-time monitoring of eruptive activity with Landsat. The small number of spectral bands, as well as their broad width in the shortwave IR (SWIR) and TIR also limit capabilities to discriminate volcanic lithologies.

### *ASTER*

The Advanced Spaceborne Thermal Emission and Reflection Radiometer (ASTER) is a medium-to-high spatial resolution, multispectral imaging system flying aboard TERRA, a satellite launched in December 1999. Volcano hazards monitoring, geology and soil mapping are specific applications for which ASTER was developed (e.g. Pieri & Abrams 2004). An ASTER scene, covering  $61.5 \text{ km} \times 63 \text{ km}$ , contains data from 14 spectral bands ranging from the VIS and NIR (VNIR; three bands at 15 m resolution), SWIR (six bands at 30 m resolution), to TIR (five bands at 90 m resolution; Abrams & Hook 2003).

A key advantage for volcanic hazard assessment is that ASTER acquires stereoscopic images at 15 m spatial resolution for deriving digital elevation models (DEMs). Specifically, in the VNIR, one nadir-looking (band 3N) and one backward-looking telescope (band 3B,  $27.7^\circ$  off-nadir with an effective viewing angle at the Earth's surface of  $30^\circ$ ) provide the stereo-pair images (Hirano *et al.* 2003). The advantage of this along-track mode of stereo-image acquisition is that the stereo-images are acquired only a few minutes apart, under uniform environmental and lighting conditions, whereas scenes from across-track data acquisition (e.g. SPOT) are several days apart (Hirano *et al.* 2003; Stevens *et al.* 2004). DEM accuracy depends on the availability, spatial distribution and accuracy of high-quality ground control points (GCPs) and on the contrast within the image (see Mauna Kea test case). Hirano *et al.* (2003) suggested that the root mean square error (RMSE) in ASTER DEM elevations ranges from  $\pm 7 \text{ m}$  to  $\pm 15 \text{ m}$ , depending on GCPs and image quality.

Processed ASTER DEMs can be acquired at the same cost as an ASTER scene (Land Processes Distributed Active Archive Center website (LPDAAC 2005); Table 1). The routine procedure utilizes the ephemeris and attitude data derived from both the ASTER instrument and the TERRA spacecraft platform to compute a relative DEM. Absolute DEMs are based on GCPs specified by the user. ASTER DEMs are derived at 30 m resolution, in an attempt to minimize errors in the

matching process. The RMSE of the relative DEM in  $x$ ,  $y$  and  $z$  is expected to range between 10 m and 30 m. An RMSE of 7–50 m is expected for absolute DEMs if at least four GCPs are provided (LPDAAC 2005). The capability of retrieving accurate relative DEMs without having to collect GCPs in the field is of great interest, especially for remote volcanoes. The exact accuracy of these DEMs still needs to be assessed, especially for high-relief terrains such as volcanoes.

The easy availability, low cost and unique combination of multispectral and 3D capabilities at 15 m resolution are the main advantages of ASTER for volcano studies. Although Stevens *et al.* (2004) demonstrated that 3D ASTER allows for accurate topographic mapping of volcanoes and highlighted the potential for volcano terrain deformation analysis by repeat DEM generation combined with spectral change analyses, the full capability of these data has not yet been fully explored. Ramsey & Fink (1999) highlighted capabilities of ASTER multispectral data in the TIR for estimating surface vesicularity contrast in volcanic rocks. ASTER multispectral data were used by Byrnes *et al.* (2004) to discriminate between different lava flow morphologies based on the spectral reflectance in the VNIR, and on the emissivity in the TIR. The main limitation of ASTER data, as with other optical RS data, for regular monitoring is their sensitivity to cloud cover, a frequent problem with high-relief subtropical volcanoes.

### SPOT

The SPOT satellites (Satellites Pour l'Observation de la Terre) combine high-resolution multispectral bands with stereoscopic capabilities. SPOT acquires data in three bands in the VNIR at 20 m spatial resolution (10 m for the most recent satellite, SPOT 5), and one panchromatic band at 10 m spatial resolution (5 or 2.5 m for SPOT 5). SPOT 4 and 5 also provide one SWIR band (20 m resolution). Despite having fewer spectral bands than Landsat or ASTER, SPOT has the advantages of higher spatial resolutions and variable viewing angles. This increases the potential temporal resolution and the chances of acquiring cloud-free images. With three SPOT satellites currently operational, it is possible to observe almost the entire planet in a single day.

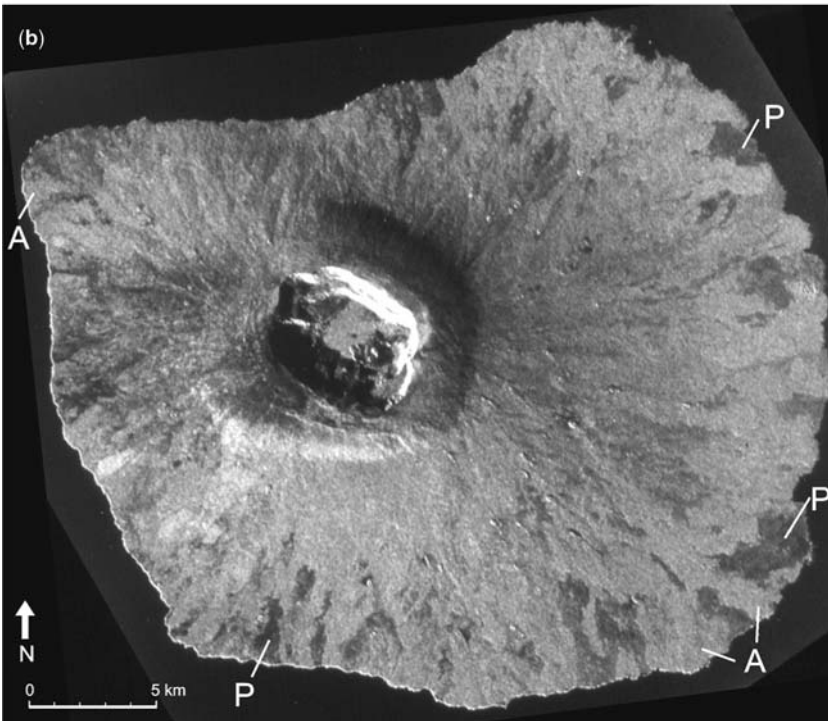
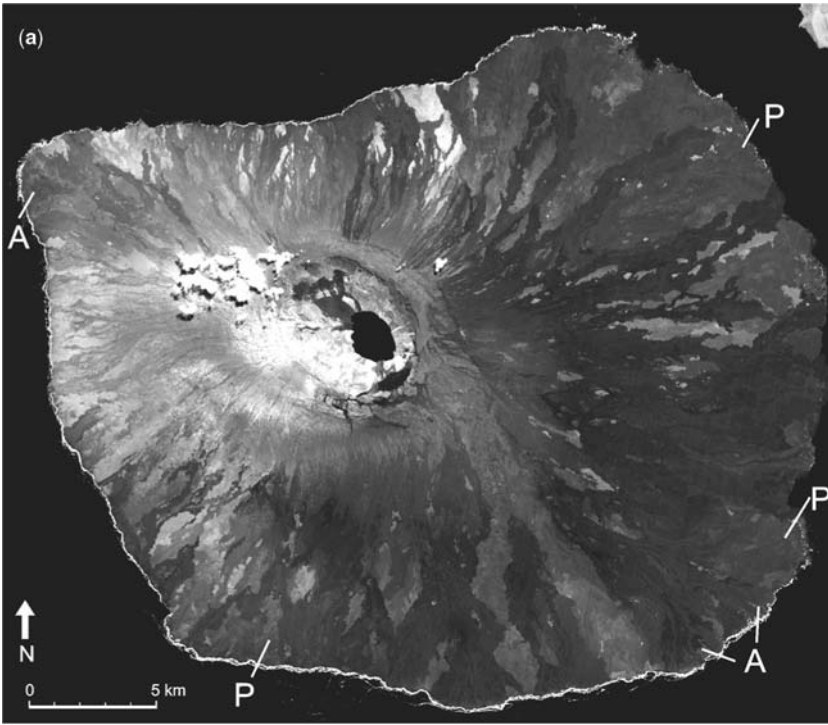
SPOT can acquire stereo-images pairs, but in cross-track rather than along-track orientation (compared with ASTER). The two stereoscopic scenes can be acquired in tandem mode on the same day by using two of the three satellites. However, the stereo-pair images are not acquired under identical illumination or atmospheric conditions. This can affect the accuracy of the resulting

DEM (e.g. vertical accuracy between  $\pm 5$  and  $\pm 20$  m; Hirano *et al.* 2003). SPOT 5, launched in May 2002, carries the High Resolution Stereoscopic (HRS) instrument, which can acquire simultaneous stereo images with 10 m spatial resolution. The simultaneity of acquisition for the stereo-pair images increases the quality of the derived DEMs (Kormus *et al.* 2004). A current problem is that the two images used to produce the DEM are not made available to users. Only the processed DEMs can be acquired. The cost of these DEMs has so far limited their applicability (Table 1).

Even though SPOT satellites have been acquiring data since 1986, applications for volcanic studies have been less frequent than those using Landsat data. The lower number of spectral bands and higher cost (e.g. a minimum of €100 per scene for European scientists, and much higher price for non-Europeans) in comparison with Landsat are the main factors limiting its current applicability. SPOT images were used to map lava flows and monitor eruptive activity at Sabancaya volcano (Chile; e.g. Legeley-Padovani *et al.* 1997), to map and assess structure and morphology of lahar deposits (see Kerle *et al.* 2003, for a review) and to map volcanic vents and lava flows, in combination with other RS and field data, at Galápagos volcanoes (e.g. Rowland 1996; Rowland *et al.* 2003). At Galápagos volcanoes, panchromatic and multispectral SPOT images allow identification of flow boundaries based on contrast in surface albedo and on surface colour change associated with flow ageing. All volcanic cones higher than a few metres were also readily identified (Fig. 1a; Rowland 1996).

### Declassified satellite images

The CORONA programme was conceived by the US Air Force and Central Intelligence Agency, to take pictures from space of the Soviet Bloc countries and other parts of the world. In 1995, a first set of images, acquired by the CORONA and ARGON systems, was declassified and made available to the public at low cost via the US Geological Survey (USGS Earth Explorer website 2005; Table 1). Between 1960 and 1972, in the operational phase, panchromatic images were recorded by a panoramic camera at flight height of c. 150 km. Depending on the sensor used, the best ground resolution varied from c. 7.3 m to 1.8 m. Satellites used on CORONA missions (sensors KH-1 to KH-4B) carried two cameras, which recorded stereo images of the Earth's surface (McDonald 1995). The principal coverage areas are Asia, Eastern Europe and Northern Africa. The filmstrips suffer from typical panoramic distortion. Time-consuming processing allows derivation



of a DEM and ortho-image from the original image (see Altairer & Christoph 2002).

A second dataset from systems GAMBIT (KH-7 surveillance system; 1963–1967) and HEXAGON (KH-9 mapping system; 1973–1980) was declassified in 2002. The KH-7 system does not offer stereo-capabilities but acquired very high resolution data (0.6–1.3 m pixel) for many specific regions including volcanic terrains of Kamchatka and Indonesia. KH-9 acquired panchromatic images over much more extensive areas with a spatial resolution of 6.1–9.2 m. When acquired in stereo-mode, successively acquired images overlap by 60%, allowing DEM derivation with standard photogrammetry techniques. In contrast to CORONA, HEXAGON images do not suffer from panoramic distortions. Because of their recent release, the capabilities of the HEXAGON data for DEM generation remain to be assessed. Although cloud cover is a limitation, a rapid search for declassified images returned potentially useful imagery for tens of active or dormant volcanoes in subtropical LDCs especially from KH4 (A and B) and KH-9 missions (USGS Earth Explorer website 2005).

The declassified satellite images provide a wealth of panchromatic, very high resolution data for many regions, including some lacking airphoto coverage. These images may offer a low-cost route to high-resolution DEM generation; for example, this option is about 3000 times cheaper than that using IKONOS data (<1 cent km<sup>-2</sup> for CORONA v. c. \$25km<sup>-2</sup> for IKONOS; Altairer & Christoph 2002). As with airphotos, CORONA data require intensive processing to correct for geometric distortions. Good quality GCPs are needed to obtain absolute elevations. Images acquired several decades ago might be of interest for assessing a volcano's morphology prior to its most recent eruptions or for studying its morphological changes.

## Satellite radar systems

### *Synthetic aperture radar (SAR)*

Radar sensors provide terrain information by recording the amplitude and phase of the backscattered signal. Amplitude and phase are influenced by radar system parameters (wavelength, incidence angle, polarization) and by terrain properties such

as surface roughness on the scale of the radar wavelength, ground slopes, and dielectrical properties of the surface (e.g. McKay & Mouginiis-Mark 1997). Different radar wavelength can be used: X-band (2.8 cm), C-band (5.6 cm; ERS, ENVISAT, RADARSAT sensors) and L-band (23.5 cm; JERS sensor). The SAR sensors (ERS-1 until 2000, ERS-2, JERS until 1998, ENVISAT, RADARSAT) differ in wavelength, looking angle and other acquisition parameters.

Radar penetrates clouds, a major advantage for the study of volcanic regions, especially in the subtropics. SAR sensors are 'active': they record their own backscattered signal, are not dependent on sun illumination, and so can work day and night; they combine ascending and descending orbit data (i.e. halving the return period from 35 days to 17.5 days in the case of ERS and ENVISAT). Radar image use for mapping is limited by the geometric distortion and shadowing effect caused by oblique viewing and topography.

Backscatter intensity has been used to map distinct pahoehoe and aa lava flow surfaces (Gaddis 1992; see below), and surface textures of lava flows generally (Byrnes *et al.* 2004). Different polarizations were also used for mapping lava flows (McKay & Mouginiis-Mark 1997). When combined with cross-validation field data, this provides insights into lava flow emplacement and constraints for lava flow modelling. Radar was also used on remote volcanoes to map new lava, debris or pyroclastic flows (Rowland *et al.* 1994; Carn 1999). Figures 1b and 2 illustrate the great capabilities of SAR datasets for volcano mapping. An SIR-C radar image of Volcán Fernandina shows how backscatter intensity varies with contrasted lava flow texture. Pahoehoe flows, which have a 'smooth' texture relative to the radar wavelength (c. 6 cm), returns a low backscatter intensity. The rougher texture of aa flows produces higher backscatter and appears much brighter. This roughness contrast is not observed on the SPOT image (Fig. 1a). SPOT and SAR data served as complementary datasets to map and characterize lava flows (e.g. Fig. 1; Rowland 1996). An ERS-1 scene acquired on Aniakchak volcano in 1992 illustrates the advantages of using SAR for assessing eruptive activity at remote volcanoes that have chronic cloud coverage limiting the applicability of optical RS (e.g. Fig. 2; Rowland *et al.* 1994).

**Fig. 1.** (a) Panchromatic SPOT image of Fernandina Island, Galápagos, collected in 1988 (10 m resolution).

Representative aa (A) and pahoehoe (P) flows are indicated. It should be noted that albedos of aa and pahoehoe flows are similar, making these surfaces difficult to discriminate even on high-resolution satellite images such as this one. (b) Shuttle Imaging Radar-C (SIR-C) image of Fernandina Island, Galápagos, collected in 1994. The smooth texture of pahoehoe lava flows (P) produces a low backscatter intensity (dark pixels). Aa (A) flows have a rougher surface, with a roughness scale of same order as the radar wavelength (bright pixels). The caldera structure, intra-caldera and flank cones are visible (see Rowland 1996, for more details).



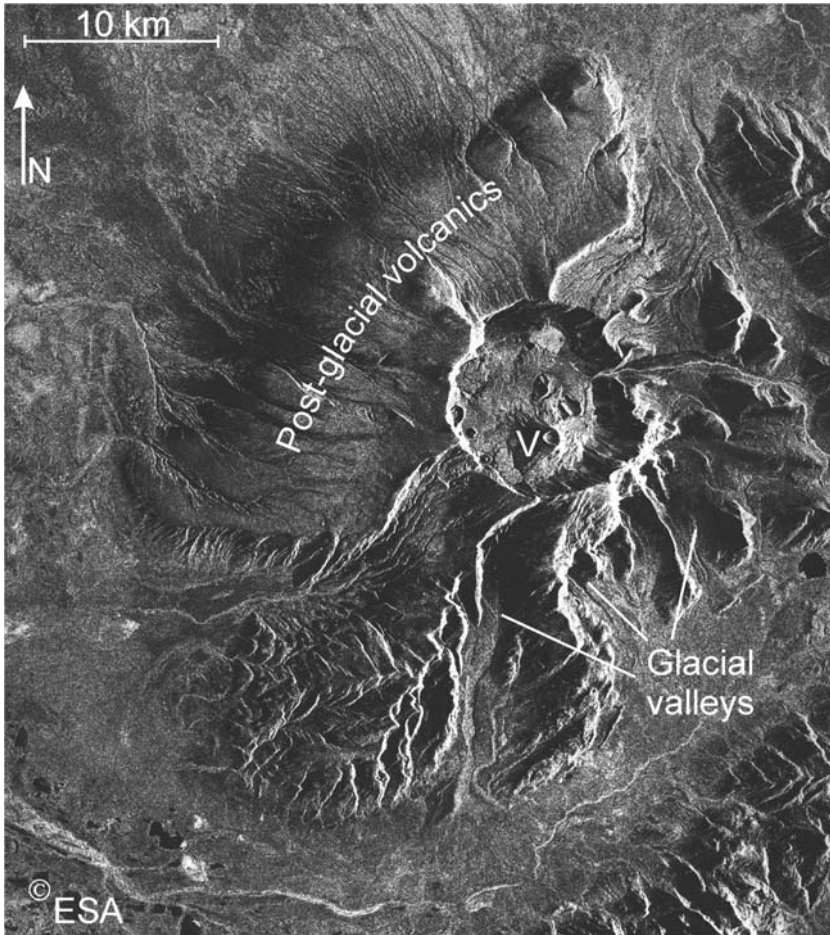


**Fig. 2.** European Remote-Sensing Satellite-1 (ERS-1) image of Aniakchak volcano, Alaska, collected in 1991. The nearly circular caldera formed c. 3400 years ago, and truncated a volcanic cone that had been glacially eroded. Post-glacial and pre-caldera(?) volcanic deposits have presumably buried glacial valleys on the north and west flanks. Vent Mountain (V) is the tallest of c. 10 intra-caldera vents. It should be noted that topographic features all appear to be steeper on their SE-facing sides. This is the effect of radar foreshortening, whereby summits and ridges are displaced toward the radar, which in this case was looking from SE to NW. (See Rowland *et al.* (1994) for additional discussion of this image.)

Careful analysis of backscatter intensity allows for recognition of post-glacial emplacement of low-mobility pyroclastic flow on the north and west flanks of the volcano. The break in slope that marks the outer limit of the flow deposit, about 10 km from the caldera rim, is highlighted by the low incidence angle of the radar beam ( $23^\circ$ ).

#### *SAR interferometry and SRTM*

InSAR has emerged as a powerful technique to derive high-resolution DEMs and study ground deformation. InSAR involves comparing the phase of the

backscatter signal for each corresponding pixel of two radar images acquired from different positions (Zebker *et al.* 2000), either at the same time by two antennas separated by a fixed baseline (e.g. SRTM or airborne), or during successive passes of a single antenna (e.g. ERS, JERS, RADARSAT, ENVISAT). InSAR gives exceptional results, although it has limitations. Preservation of the phase coherence (i.e. the level of correlation between the images of an interferometric couple) is the most limiting factor. Coherence is controlled by the system geometry (Zebker & Villasenor 1992) and by changes in surface conditions at the scale of the radar wavelength (c. 1–20 cm) during the time interval separating

acquisition of the two images. Dense vegetation causes rapid coherence loss for data acquired in C-band (Kervyn 2001) but not L-band (Stevens & Wadge 2004). Decorrelation (i.e. loss of coherence) can also be used positively to map new lava flow areas in regions with an overall good coherence conservation (Lu *et al.* 2003).

As far as the surface 'stability' is concerned, the shorter the period between the two acquisitions, the higher the coherence will be. This is the main motivation for single-pass interferometry, such as in the recent SRTM mission (Rabus *et al.* 2003). On the other hand, a repeat-pass configuration offers more flexibility, particularly regarding the geometry of the acquired data. Depending on the application, one can look for a pair of images offering the optimum geometric baseline (i.e. spatial distance between the two points in space from which the two images were obtained, projected perpendicularly to the line of sight), incidence angle, orbit mode and revisiting rate. If the goal is to derive topography, a long geometric baseline is preferable; the phase difference will be associated with a smaller difference in elevation (e.g. Zebker *et al.* 1994). A shorter geometric baseline is more suitable for ground deformation studies. In this case, a phase difference is also produced by the displacement of the surface; deformation studies require that the 'topographic phase' is filtered out.

Although radar can penetrate clouds, a phase delay can still occur that must be taken into account for data interpretation. Differential interferometry (DifSAR) has to discriminate between the various phase difference origins, such as geomorphology, atmospheric conditions and ground deformation (Massonnet & Feigl 1995).

### *InSAR monitoring*

The contribution of InSAR to monitor volcanic activity is particularly important in areas where cloud coverage is common and where deformations are recorded (e.g. Zebker *et al.* 2000; Stevens & Wadge 2004). However, monitoring is inherently time-related and coherence loss can prevent the use of 'conventional' DifSAR in the long term or for areas with dense vegetation. Recent developments make use of the persistent scatterers (PS) technique. Isolated targets in a highly decorrelated pair may still preserve phase coherence and be used to retrieve ground deformation, provided the PS density is high enough (Ferretti *et al.* 2001). The PS method, which requires a large number of scenes (>15, ideally >30), has proved highly successful and accurate in urban areas where hundreds PS km<sup>-2</sup> can be identified (Ferretti *et al.* 2004). Hooper *et al.* (2004) proposed an adaptation of

the method for natural areas devoid of such urban-type permanent scatterers.

Airborne InSAR (e.g. AirSAR; AirSAR Jet Propulsion Laboratory website 2005) has been used to produce repeated high-resolution DEMs over volcanic terrains, to study volcano morphology, assess morphological changes or to constrain the volume of newly erupted material (Rowland *et al.* 1999, 2003; Lu *et al.* 2003). So far, these applications have, however, been limited to volcanoes in Hawai'i, Alaska, the Aleutians and New Zealand (Stevens *et al.* 2002).

### *SRTM and InSAR topography*

The Shuttle Radar Topography Mission (SRTM) flew on the Space Shuttle Endeavour in February 2000. Using two radar antennas separated by a 60 m long mast, it collected single-pass DEM data over nearly 80% of Earth's land surfaces (i.e. between 60°N and 56°S), using both a C- and X-band radar. The 11 day mission generated the most complete high-resolution digital topographic database for Earth. For the USA, the processed C-band DEM data have been released at 30 m spatial resolution (1 arc second). For the rest of the world, SRTM C-band DEMs are available only at 90 m spatial resolution (3 arc second). The nominal absolute horizontal and vertical accuracies are ±20 m and ±16 m, respectively (SRTM mission, JPL website 2005), although within a single scene the relative accuracies are considerably higher (Rabus *et al.* 2003). Table 2 shows the proportion of historically active and Holocene volcanoes for which SRTM DEMs at 30 or 90 m resolution are now available.

**Table 2.** Illustration of how different fractional areas of the Earth with historically active and Holocene volcanoes are best covered by near-global digital elevation models

	Historical	Holocene	Total
SRTM 30 m (%)	7.8	10.4	9.4
SRTM 90 m (%)	76.6	82.6	80.2
GTOPO30 1 km (%)	5.3	4.2	4.6
No data (%)	10.2	2.9	5.8
Number of volcanoes	561	840	1401

C-band SRTM 30 m data are available for the USA (including Hawaii and Alaska). SRTM 90 m data are available for all land surfaces between 60°N and 56°S. The 1 km resolution GTOPO data are available for all land surfaces (Global Topographic Data). No data: submarine and subglacial volcanoes for which there is no global coverage data at high resolution. Data on volcano location and activity are from Simkin & Siebert (1994; updated list available from Global Volcanism Program—Smithsonian Institution 2005).

The potential of gaining understanding about how volcanoes work, hazards or what controls volcano morphology and growth with SRTM data is tremendous. What controls the diversity, variability and complexity of volcano morphology has not been studied systematically. The only textbook on the subject dates from the 1940s (Cotton 1944). A considerable amount of novel work is now expected, exploring what can be learned from the shape, size and vent distributions of volcanoes.

Because of their shorter wavelength, the X-band DEMs have a higher relative height accuracy (i.e. within a scene) by almost a factor of two. The X-band dataset has been processed and is available at a 25 m spatial resolution. The X-band DEMs do not cover the entire globe (i.e. *c.* 25% of C-band SRTM data coverage is not covered by the X-band SRTM; the areas not covered are evenly distributed worldwide). Another limitation is the €400 per scene cost of the X-band DEMs (X-SAR SRTM website 2005).

### Mapping topography with ASTER

Topographic maps at 1:50 000 scale or larger are not available for many regions, especially in developing countries. In the framework of a large mapping project of the Drâa valley (Morocco; Drey *et al.* 2004), Goossens *et al.* (2003) took advantage of the high-resolution and 3D capability of ASTER and CORONA data to derive a topographic map for a region where the best available maps were at 1:100 000 scale. This case study, albeit in a non-volcanic terrain, is summarized here to illustrate the capabilities of the method.

Using a limited number of high-quality GCPs (10 and 7, respectively, for the two scenes used) collected with a differential GPS (TRIMBLE Pathfinder Pro XRS), ortho-photomaps were produced for two areas based on two ASTER scenes. The RMSE on the GCPs in the  $x$ ,  $y$  directions was *c.* 1 pixel (*c.* 15 m), whereas the vertical RMSE was 5 m and 10 m, respectively, for the two scenes. The field campaign illustrated that high-quality GCPs that can be accurately located on the satellite image are difficult to find in regions with little human infrastructure and a monotonous landscape (e.g. most volcano landscapes). Comparison between the new DEM and existing topographic map shows that the ASTER-derived contour lines closely match available information on the 1:100 000 topographic map. More detailed contour lines with a smaller elevation interval were generated (20 m instead of 50 m intervals; Fig. 3a and b). The ortho-photomap (Fig. 3a and b) has a 15 m resolution and provides more information than the existing map. ASTER has the

advantage that, with a limited number of GCPs, a DEM covering a zone of  $60 \times 60 \text{ km}^2$  can be readily generated.

Figure 3c and d illustrates the orthomaps with contours obtained by processing a pair of CORONA stereo-images for the same region at a spatial resolution of 4 m. Based on 15 GCPs collected with a Leica 300 Differential global positioning system (accuracy of 5 cm) the resulting topographic map has a 1:10 000 scale. The DEM vertical accuracy is *c.* 20 m (Schmidt *et al.* 2002). These products are of much higher resolution than the 1:100 000 scale topographic maps that were the only ones available in this area. These two methods are thus especially suitable for mapping purposes in areas where no accurate topographic maps exist. This is the case for many volcanic regions. Collection of high-quality GCPs with a homogeneous spatial distribution on the satellite image is a key factor for the systematic production of orthophotomaps over hazardous volcanic terrains.

### Case study: Mauna Kea, Hawai'i

To assess and compare capabilities of the above-mentioned RS data types, data were collected for Mauna Kea volcano, Hawai'i. The goal was to compare information retrieved from satellite datasets with analyses of airphotos and topographic maps. We focus on the fine-scale capabilities of the different datasets to provide quantitative morphological data on the scoria cones on Mauna Kea's flanks.

Pyroclastic constructs are the most common on-land volcanic landforms on Earth (Riedel *et al.* 2003). They range in size from spatter mounds only a few tens of metres wide, formed by low-energy eruption, to scoria cones several kilometres in diameter and hundreds of metres high. Cone-building eruptions (Riedel *et al.* 2003) are explosive, can be associated with high-rising ash clouds and widely dispersed ash, and pose a threat where cities are built on cone fields (e.g. Mexico City). Recent cone-building eruptions led to evacuations of settlements, building collapses (e.g. Heimaey, Iceland, 1973), or airport closures (e.g. Catania, July 2001 Etna eruption).

The morphology of small-scale pyroclastic constructs can be described by average values of crater width  $W_{\text{cr}}$  and construct height  $H_{\text{co}}$  relative to basal cone diameter  $W_{\text{co}}$ . Previous studies, based on a limited number of cone fields, found typical  $W_{\text{cr}}/W_{\text{co}}$  ratios of 0.40 and  $H_{\text{co}}/W_{\text{co}}$  ratios of 0.18 for pristine cones. However, published datasets (e.g. Wood 1980a) and preliminary results of the present study suggest a wide variability in these ratios. Riedel *et al.* (2003) gained insights into cone-forming eruptions and hazards by developing

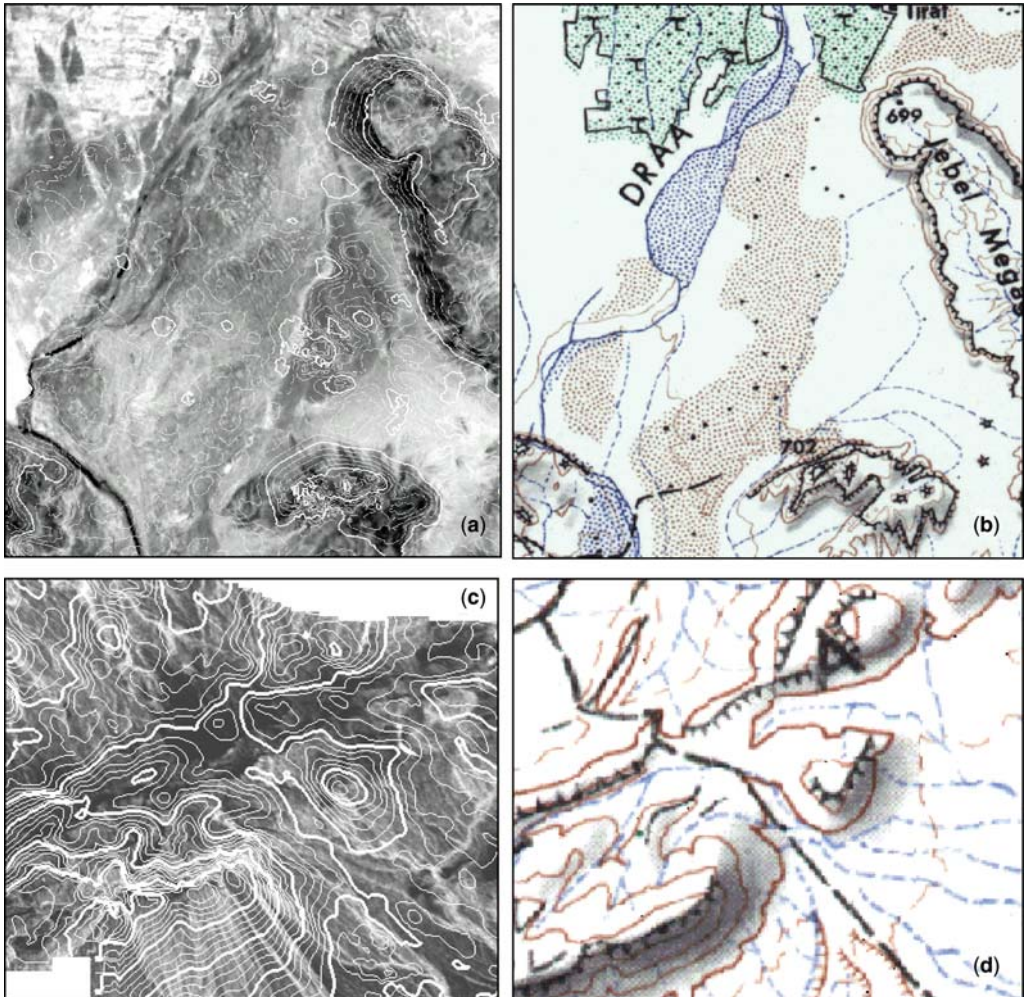


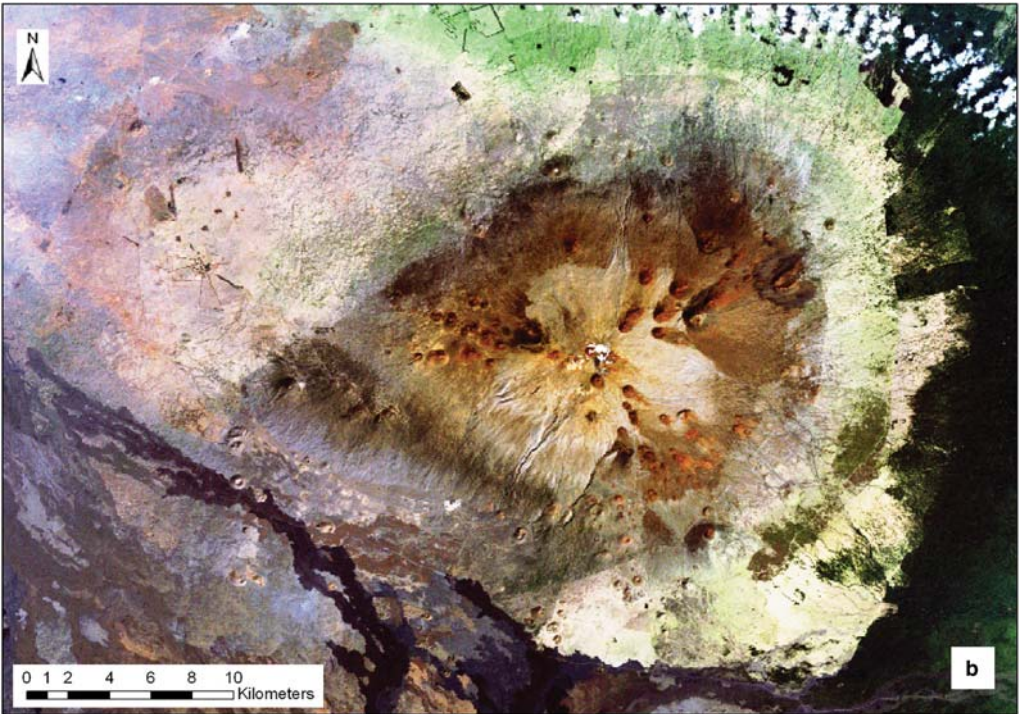
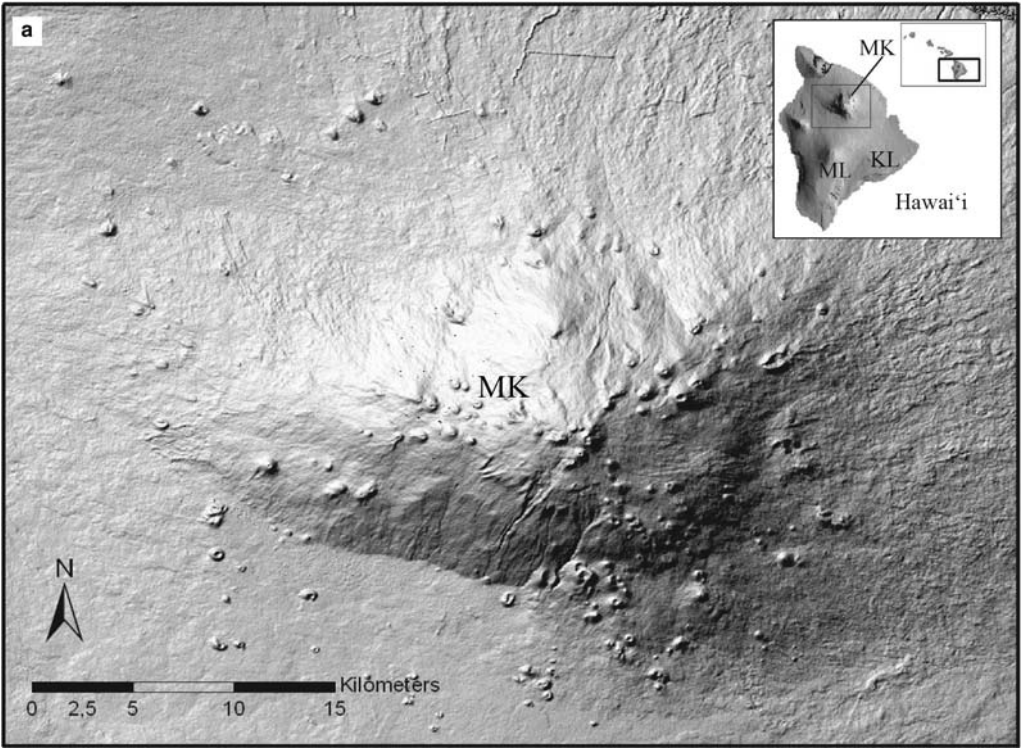
**Fig. 3.** (a) Topographic ortho-photomapped derived from subset of ASTER scene of the Drâa valley (Morocco). (b) Subset of 1:100 000 topographic map for same region (adapted from Goossens *et al.* 2003). (c) Topographic ortho-photomapped derived from CORONA data of the Drâa valley (Morocco). (d) Subset of 1:100 000 topographic map for same region (adapted from Schmidt *et al.* 2002).

a capability of inverting volcanic construct shape and size data to derive key eruption parameters.

Some previous studies focused on identifying pyroclastic constructs from airphotos or satellite imagery to document volcanic vent spatial distribution and assess tectonic controls (e.g. Chagarlamudi & Moufti 1991; Connor & Conway 2000). Davis *et al.* (1987) used the specific spectra of iron-oxidized scoria to discriminate basaltic pyroclastics from lava flows. All the above-mentioned studies concluded that RS data, usually Landsat imagery, allow to identify 60–80% of the pyroclastic constructs within a cone field. Rowland (1996) identified most of the pyroclastic

cones on Volcán Fernandina (Galapagos Island) by combining a TOPSAR-derived DEM and a panchromatic SPOT image. The latter analysis failed to identify only very small arcuate vent constructs (1–3 m high).

Mauna Kea lies in the northern half of the Big Island of Hawai'i (Fig. 4). Activity in the last 130 ka or so has been marked by numerous small gas-rich eruptions that formed *c.* 300 scoria cones (Porter 1972). Mauna Kea most recently erupted *c.* 4000 years ago (Wolfe *et al.* 1997). It was chosen as a study site because of the high density of pyroclastic constructs, the morphologies of which had already been partially documented by



Porter (1972). The cones have a wide size range ( $W_{co}$  from *c.* 15 to 1450 m) and small average size (median diameter 450 m) compared with other cone fields (Wood 1980a), which makes them ideal to evaluate the limitations arising from the spatial resolution of the diverse RS data sources. Traditional sources of spatial data (aerial photographs, topographic and geological maps) were available to compare with our observations and to cross-evaluate RS quantitative measurements. The Mauna Kea cone field, extending from 750 to 4208 m above sea level (a.s.l.), a *c.* 3500 m elevation range, spans a wide range of climatic conditions and vegetation zones. The contrast in conditions and construct ages (from 150 ka to 4 ka) allows us to assess the general applicability of the approach to volcanic fields and the limitations of several recently developed RS mapping methods.

#### *Data sources and visual interpretation*

A Landsat ETM+ image, processed to level L1G (radiometric and systematic geometric corrections applied; Williams 2003) was freely downloaded from the Global Land Cover Facilities website (2005; Table 1). The data were acquired by the satellite on 5 February 2000, and cover the NW part of the Big Island of Hawai'i (Fig. 4b). An ASTER-level 1B image (i.e. registered radiance at sensor with automatic radiometric and geometric correction applied, similar to Landsat L1G; Abrams & Hook 2003) acquired on 5 December 2000 was freely downloaded from the Land Processes Distributed Active Archive Center website (LPDAAC 2005; Table 1). Clouds in the ASTER scene required that we exclude *c.* 50 cones of the *c.* 300 Mauna Kea cones (i.e. to have a cloud-free sub-scene for digital photogrammetry processing). SWIR bands of the ASTER scene contained significant 'linear' noise. This is the commonly observed ASTER SWIR crosstalk problem (see ASTERGDS website 2005). C-band SRTM DEMs at both 30 m and 90 m resolution were freely downloaded from the Seamless Data Distribution System (2005, Table 1). The 90 m resolution is used here to exemplify what is achievable for volcanic regions outside the USA.

The ASTER scene (bands 3 N and 3B) was processed using Virtuozo digital photogrammetry software, producing a DEM with 11 GCPs extracted from 1:24 000 scale topographic maps. The

processing provided georeferenced and orthorectified images in the three VNIR bands. Several DEMs were produced by varying the DEM spatial resolution and the level of details in the matching process. The user needed to specify the spatial interval (i.e. number of pixels) between two pixels that are automatically matched by the software. Elevations were estimated only for matched pixels and extrapolated in the specified interval. Setting a finer-matching resolution results in more matching errors. In contrast, setting a coarser-matching resolution produces a smoother DEM.

The vertical RMSE of the 11 GCPs was *c.* 4 m, whereas the horizontal RMSE for these points was *c.* 20 m. The few points for which exact elevations were provided on the topographic maps typically corresponded to points (e.g. summit of cones) that could not be exactly located on RS images (error of 1 pixel unavoidable). A trade-off had to be found between the high resolution needed in the matching process to render small topographic features (e.g. scoria cone craters) and the increasing editing work needed to correct for matching errors. The ASTER DEM generation procedure takes a few hours, but several days can be spent on fine matching–editing (i.e. manually matching pixels for areas where the automated process generated errors). Here, matching at too fine a level generated troughs or peaks (i.e. a cluster of pixels with abnormally low or high elevations compared with their surroundings) in regions with low contrast. Optimal results were obtained for a matching interval of 3 pixels (45 m) and 30 m spatial resolution. No manual editing of the matching process was undertaken. To reduce errors for regions where the resulting DEM computed slope angles above 45° (i.e. the upper limit expected on Mauna Kea), the pixel elevation was replaced by that from a DEM processed with a matching interval of 7 pixels.

The accuracy of the SRTM and ASTER DEMs was evaluated using a 10 m resolution DEM interpolated from digitized contour lines of the topographic maps. The preliminary comparison of the ASTER and SRTM DEMs led to slope aspect-controlled errors, later attributed to errors with georeferencing of the SRTM DEM. This systematic error was only identified and corrected thanks to the DEM derived from the topographic map. Subtracting the topographic map-derived DEM from the ASTER one, we obtained a mean absolute

**Fig. 4.** (a) Shaded relief of Mauna Kea cone field derived from the 30 m resolution SRTM DEM (sun azimuth 315°; sun elevation 80°; elevation exaggerated by factor of three). Inset shows the Big Island of Hawai'i and locations of Mauna Kea (MK), Mauna Loa (ML) and Kilauea (KL). (b) True colour composite of the Mauna Kea cone field from the Landsat ETM+ image (R: band 3, 0.63–0.69  $\mu\text{m}$ ; G: band 2, 0.53–0.61  $\mu\text{m}$ ; B: band 1, 0.45–0.52  $\mu\text{m}$ ). White patches on the upper right are clouds, and a small snow patch covers the summit cones. Lava flows to the SW are recent Mauna Loa flows. The arcuate fault-like volcano-scale feature extending from SSW to NNE and 'passing through' MK summit should be noted.

**Table 3.** Results of the error analysis of the ASTER and SRTM DEMs (30 m resolution) compared with the DEM derived from topographic map for Mauna Kea volcano

	DEM's		
	ASTER; 11 GCPs	ASTER; 13 GCPs	SRTM 30
Mean absolute difference (m)	17	11	6
Vertical RMSE (m)	21	13	9

The mean absolute difference is obtained by subtracting DEMs. The vertical RMSE is assessed using a large number of randomly selected points. Original ASTER DEM processing was performed using 11 GCPs. The addition of two GCPs improved the accuracy of the DEM.

difference of 11 m (90% of the errors ranging between  $-18$  and  $+29$  m). Based on 218 control points selected randomly within the study area and taking the topographic map–DEM as a reference, we obtained a vertical RMSE of 13 m. This error is in agreement with results from previous studies (Hirano *et al.* 2003). Errors are attributed to the large altitude range, low spectral contrast in band 3 (near-IR) for the Mauna Kea summit region, and especially to a lack of precise GCPs there. It should be noted that a mean absolute difference of 17 m and an RMSE of 21 m were obtained in a first attempt. Large errors were located in the northern part of Mauna Kea. Significantly, the accuracy of the overall DEM was drastically improved by adding two GCPs on the northern flank (Table 3). Overall, the ASTER DEM tended to underestimate elevations on the higher region of

Mauna Kea and to overestimate them in the vegetated lower region. This is consistent with the fact that topographic maps are providing ground elevation value, whereas the ASTER and SRTM DEMs provide an average elevation for the vegetation canopy.

Based on a sample of 450 control points selected randomly on the topographic map–DEM, we obtained an RMSE of 9 m for the SRTM dataset. The mean absolute difference over the entire cone field is 6 m (90% of the errors ranging between  $-11$  and  $+18$  m; Table 3). We cannot exclude that part of this is error in co-referencing the two DEMs. Most pixels for which the SRTM DEM overestimates elevation by more than 10 m are located in the heavily forested regions east of the summit.

Shaded relief, oblique 3D views, and slope maps were generated from the SRTM and ASTER DEMs

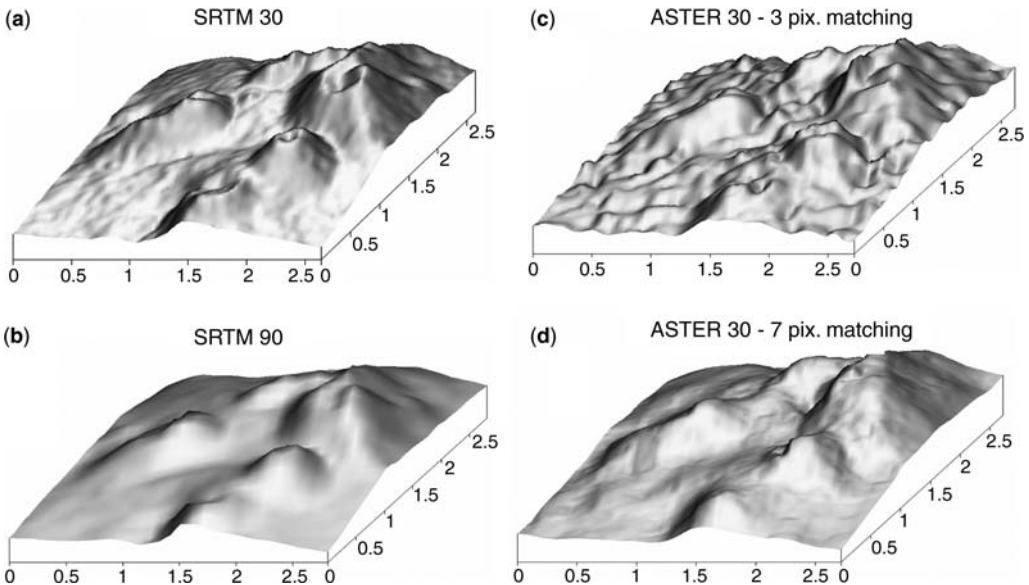


**Fig. 5.** Oblique view of shaded relief of the Mauna Kea summit displaying five cinder cones. (a, b) 30 m and 90 m resolution SRTM; (c, d) 30 m resolution ASTER DEM, the stereo-pair of images being matched every 3 and 7 pixels, respectively.

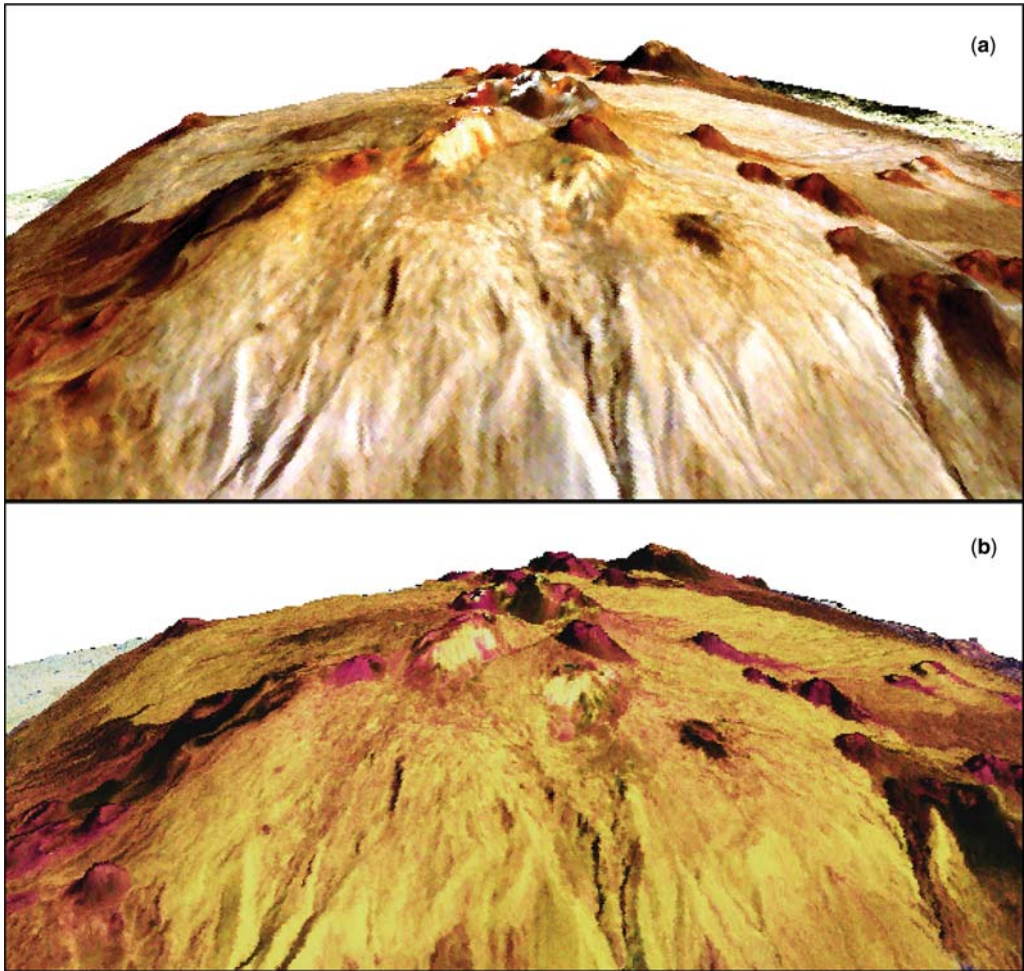


**Fig. 6.** (a) True colour composite of Landsat ETM+ bands draped over the 30 m SRTM DEM. (b) Colour composite of the three VNIR ASTER bands draped over the 30 m ASTER DEM.

in a geographical information system (GIS; ArcMap 8.1) for visual interpretation (Figs 4–6). The shaded relief view of the entire cone field (Fig. 4a) shows the high cone density and clustering in three main zones radiating away from the Mauna Kea summit, described as ‘rift zones’ by Porter (1972). The steep upper flanks are also clearly visible. The ASTER-derived DEMs likewise generated an accurate overall picture of the volcano morphology, although small-scale surface irregularities (i.e. noise in the data) limit identification of small topographic features, such as craters. Figure 5 compares oblique, SRTM- and 3D ASTER-derived views of the Mauna Kea summit cones. The 30 m spatial resolution SRTM DEM allows identification of individual cones and delineation of crater rims. At 90 m resolution, SRTM provides a much

smoother representation of the topography. The smaller cones cannot be identified as specific features and craters can no longer be delineated or are no longer apparent. The ASTER shaded-relief DEM image, although at the same spatial resolution (30 m), is visually less attractive than that of the 30 m SRTM because of small-scale irregularities in the topography. From comparison with aerial photographs, these irregularities can be attributed to artefacts introduced through errors in the automated matching process. Nevertheless, small volcanic features and the largest craters can be recognized. Landsat colour composites (e.g. true colour, Fig. 4b) allow identification of volcanic features, contrasting vegetation cover, and volcanic and sedimentary surfaces such as glacial deposits in the Mauna Kea summit area.



Figure 6 illustrates the advantage of combining spectral data of a colour composite image and topographic data. The Landsat true colour composite draped over the SRTM DEM helps discriminate between cones, ash deposits and glacial moraines. To obtain a correctly draped image, georeferencing of the Landsat image had to be manually corrected using tie points, as it was offset by 200 m to the west. ASTER has the advantage that its spectral and topographic data are retrieved from the same dataset (and are therefore co-registered). The finer spatial resolution of the VNIR spectral bands (15 m) and the 30 m resolution ASTER DEM provide a combined high-quality volcano rendering. The comparison with an airphoto of the Mauna Kea summit with similar viewing conditions (Fig. 7) illustrates the level of detail that can be obtained through combination of multispectral (ASTER or Landsat) and topographic data (SRTM DEM or ASTER DEM).

Visual analysis of integrated optical and topographic data proved to be the best easily available RS product to map small-scale volcanic features. It also identified a major arcuate structural feature, currently a focus of study, relating to volcano-scale spreading. The arcuate feature is incised by deep

valleys extending in the NNE and SSW upper flanks of Mauna Kea, and passing through the summit where the valleys join and are widest (Fig. 4). We interpret this as a superficial graben from volcano-scale spreading in a preferential WNW–ESE direction as a result of Mauna Kea's load over a mechanically weaker layer (Merle & Borgia 1996). Other, less well-defined graben structures, extending radially from the summit, are consistent with a volcano spreading interpretation. Directional spreading can be explained by the fact that the volcano is not buttressed by other large edifices in the WNW–ESE direction. This example illustrates how integration of topographic and multi-spectral RS data allows identification of major structural features that were not identified through field work or airphoto interpretation.

#### *Morphometry of small-scale volcanic structures of Mauna Kea*

Cone morphometry parameters were independently collected from the Landsat scene, ASTER-derived DEM draped with ASTER VNIR bands, SRTM DEM and topographic maps. First we assessed the capabilities of each of these datasets to identify

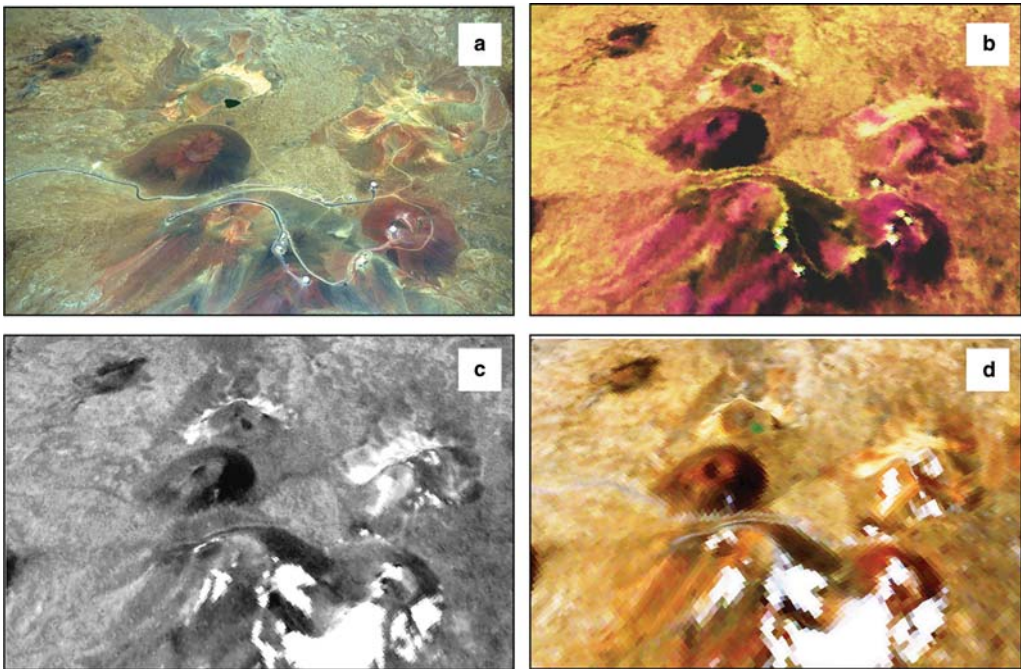


**Fig. 7.** Oblique view of Mauna Kea summit from north. (a) Colour airborne photography; (b) colour composite of the VNIR ASTER bands draped over the 30 m ASTER DEM; (c) 15 m resolution Landsat ETM+ panchromatic band and (d) colour composite of the three VIS Landsat ETM+ bands draped over the SRTM DEM at 30 m resolution. White areas in the bottom part of (c) and (d) are summit cones covered by snow.

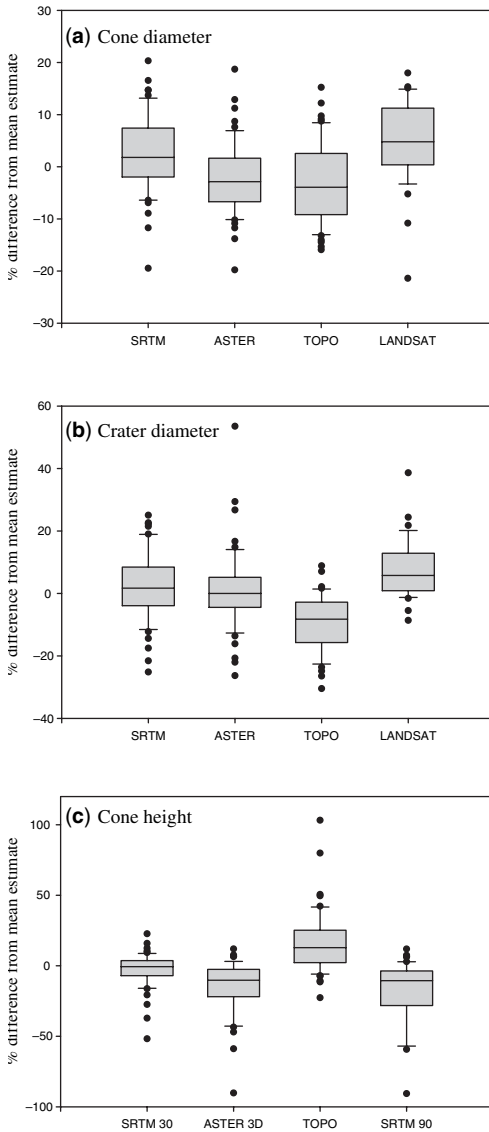


**Fig. 8.** Comparison of cone diameter (a), crater diameter (b), and cone height (c) estimations from four different data sources. The boxes illustrate the range of differences between estimates and the mean estimated value from all the datasets (SRTM 90 m not considered in (c) for average calculation). The vertical line in each box is the median of the distribution. The extent of each box includes 50% of the data around this median value. Horizontal lines above and below each box indicate the 90th and 10th percentiles. Outliers are plotted as separate dots. Datasets: SRTM, SRTM 30 m DEM; ASTER, combined DEM and multispectral imagery; TOPO, estimate from paper topographic maps; LANDSAT, estimate from Landsat ETM+ multispectral imagery; SRTM90, SRTM 90 m DEM.

pyroclastic constructs and vents, using the geological maps as a validation source. Pyroclastic constructs of the Mauna Kea cone field were identified by their common positive topographic relief. Importantly, specific spectral features of oxidized scoria also helped by allowing identification of constructs with little or no topographic relief and limited spatial extent (Davis *et al.* 1987). Quantitative parameters (e.g. namely the cone and crater diameters, the construct height, and the mean and maximum outer slope) were retrieved for all identified cones (*c.* 220) from the topographic maps and from the Landsat scene (i.e. elevation and slope estimates from topographic maps only). The same parameters were retrieved for a subset of 50 cones covering the entire range of cone sizes and shapes from the ASTER dataset and from the SRTM DEM. For the topographic maps, horizontal and vertical error ranges of *c.* 24 and 12 m, respectively, are expected as a result of small measurement errors and ambiguity in cone base location between two contour lines. For the RS datasets, an error range of 1 pixel (*c.* 15–30 m) is expected. The detailed volcanological interpretations will be the subject of another paper. Here we focus on methodological aspects and on comparison of the errors affecting the estimated parameters.

The geological map used as the validation dataset shows 310 vent constructs on Mauna Kea. Constructs that are not systematically detected as small volcanic features on the topographic and RS datasets are invariably those with a very limited spatial extent (<200 m), low height (<20 m) and no distinctive spectral expression. Most are interpreted as spatter mounds and ramparts. Several of these deposits are mapped as highly elongated features, the result of fissure eruptions. These constructs are usually less than 15 m high (e.g. Riedel *et al.* 2003). Several processes may conceal the original ‘truncated cone’ construct morphology, including intense weathering, compaction, mass wasting, and subsequent coverage of the lower slopes by lava flows or later pyroclastic products. These types of deposits, lacking a topographic expression, can only be identified by the combined use of high-resolution aerial photography and field work.

All the datasets allowed us to identify pyroclastic constructs with near-equal success. Ninety-five percent of the scoria cones (cone base >250 m) less than 70 ka old were identified and mapped for each dataset. Between 65 and 72% of all vents (i.e. including not only cone vents but also some small metre-scale vents along fissures) were unambiguously identified. Although the average vent construct size on Mauna Kea is small relative to other cone fields in the world (Wood 1980a), the above-mentioned results are similar to those

obtained by previous RS mapping of volcanic cones (e.g. Davis *et al.* 1987; Chagarlamudi & Moufti 1991). The constructs that could not be mapped were small spatter constructs ( $W_{co} < 250$  m) and a few larger cones (300–800 m diameter deposits on the geological map) whose morphology has been obliterated by erosion and by later lava flows. Topographic maps and the Landsat image allowed similar results to be derived: 230 and 220 pyroclastic constructs were identified, respectively, from these data sources. However, only 199 of these could be simultaneously identified and mapped on both topographic maps and Landsat imagery. Cloud and snow cover are important factors that prevent cone mapping on the Landsat (or ASTER) image. Another limitation is the moderate spatial resolution of Landsat data, which hinders recognition and/or delineation of constructs less than 150 m wide with no specific spectral expression. Several pyroclastic features could not be recognized on the topographic maps because of the lack of distinct positive topography, but could be mapped on the satellite imagery by taking advantage of the high MIR reflectance typical of near-vent oxidized volcanic products (i.e. red scoria or spatter).

The SRTM DEM allowed unambiguous identification of 218 of the 320 pyroclastic constructs. As with the Landsat data, the 30 m spatial resolution hindered recognition of the smallest constructs (those with width  $< 200$  m). The fact that the SRTM elevations correspond to the average height of the vegetation canopy also causes ambiguities in cone identification in places with discontinuous forest coverage. Small positive relief features can indeed be created by locally higher vegetation (e.g. a small forest in otherwise non-forested area). Ambiguity can be resolved by combining the SRTM DEM and multispectral data.

The ASTER DEM allowed recognition of 171 out of 260 mapped pyroclastic features within the area covered by the ASTER scene (a success level of 65%). This poorer result is explained by the fact that the ASTER scene includes only the summit region, which happens to contain most of the small-size spatter mounds. We conclude that the ASTER dataset (i.e. multispectral data and ASTER DEM) has a capability similar to the three other datasets for mapping Mauna Kea pyroclastic constructs. The availability of good quality SWIR bands combined with an ASTER-derived DEM constrained by high-quality GCPs would further improve the mapping capabilities of the ASTER data.

### *Quantitative morphological parameters*

For all the Mauna Kea constructs identified on the topographic maps and Landsat scene, the basal

diameter,  $W_{co}$ , was estimated (i.e. computed as the diameter of a circle having an area equivalent to that of the cone base). Results from the two datasets were similar over the entire cone field. On average,  $W_{co}$  estimates derived from the Landsat image are c. 40 m greater than those derived from topographic maps. However, differences range from  $-80$  m (underestimation of Landsat-derived  $W_{co}$  relative to the topographic map-derived estimate) to 280 m. For 66% of the features, this difference ranges between  $-20$  and  $+80$  m. A key result is that the magnitude of the discrepancy is not dependent on construct size, but rather on the degree of irregularity of the cone outline. Using the geological map as a validation reference, a comparison of the spatial extent of each feature between the Landsat and topographic map datasets was undertaken for 75 features for which discrepancies in  $W_{co}$  values were high. For 40 cones the Landsat-derived  $W_{co}$  was found to be more accurate than the topographic map-derived value. Importantly, the results from the topographic map were usually ambiguous because of the lack of a well-defined basal break in slope for those cones. In only eight cases were the cones less accurately delineated with the Landsat data. This was due to misinterpretation of the cones' spatial extent, as a result of vegetation cover or absence of topographic information. The last 27 cones were very small features ( $W_{co} < 200$  m) and the estimate from the geological map was halfway between those from the topographic map- and Landsat-derived estimates. The average 40 m discrepancy between estimates from the two data sources is to be expected. It falls within the estimated error ranges for the two estimates. Considering the 1:24 000 scale of the topographic map and the finite spatial resolution of the image, errors of c. 30 m are not abnormal, and a slightly larger error is likely to be related to limitations associated with defining the cone extent in those cases where the break in slope delimiting the cone base is not sharply defined.

Figure 8a illustrates the differences in cone base estimates from the four datasets for a subset of 50 cones. On average, all the datasets lead to similar cone size estimation, even if major discrepancies do sometimes occur as a result of misinterpretation in the spatial extent of the cones. The box-plots illustrate that for all the datasets, more than 50% of the estimates are within 10% of the mean estimate (i.e. average of the estimates from the four datasets). The same observation holds for the crater size estimation, although a larger relative error range is observed. Figure 8a and b suggests that topographic maps, with no spatially continuous data coverage, tend to lead to underestimated cone size values, whereas the opposite is true for the Landsat image, which lacks topographic

information. Both the ASTER and SRTM datasets lead to estimates that are generally close to the average value. The discrepancy range is the smallest with ASTER, thanks to the combined use of multispectral and topographic data, although some large errors are obtained for a few cones for which the spatial extent of the cone and/or crater is ambiguous. These results suggest that reasonably accurate quantitative morphology description through  $W_{cr}/W_{co}$  ratios can be derived from any one of the datasets assessed here.

The height of volcanic cones is of interest because it is controlled both by the cone age (Wood 1980*b*) and by cone particle characteristics (Riedel *et al.* 2003). The height of 50 Mauna Kea scoria cones was estimated by subtracting the average cone base elevation from the average crater rim elevation. Results were independently extracted from the topographic maps, SRTM and ASTER DEMs. Results (Fig. 8c) illustrate that SRTM provides the smallest discrepancies (i.e. difference from the average of the three results). Elevations on topographic maps were recorded at only four locations each for the base and crater rims, and topographic map cone height estimates tend to be higher than the average. For 70% of the cones, the heights from the ASTER DEM are between 80 and 110% of the average estimated height. For constructs <50 m high (25% of the constructs), ASTER DEM height estimates are as much as 50% less than the average estimate. Although the ASTER-derived DEM has a lower vertical accuracy than the SRTM DEM, it still provides reasonable cone height estimates for large constructs ( $H_{co} > 60$  m). Finally, it should be noted that the capabilities of the SRTM dataset would be greatly reduced if it were available only at 90 m spatial resolution (as is the case for non-USA locations; see Fig. 8c). The cone height estimates are significantly lower with the 90 m SRTM and the range of discrepancy compared with the average value is larger.

### Rungwe Volcanic Province case study

Many volcanoes in developing countries remain poorly known and it is typically difficult to acquire good-quality maps and airphotos for them. Satellite RS allows us to rapidly explore volcano morphology and identify evidence of recent activity (e.g. Dubbi volcano, Ethiopia; Wiart *et al.* 2000). The Rungwe Volcanic Province illustrates the type of information that can be retrieved from different RS datasets, including SRTM DEM, multispectral datasets and SAR interferometry. The objective here is to illustrate what can be done with RS, including deriving hazard-relevant information

that can be evaluated in the field, as well as to highlight some remaining challenges for RS.

The Rungwe Volcanic Province lies at the intersection of the west, east and south branches of the East African Rift in SW Tanzania (Fig. 9). The most recent eruption in the province was at Kiejo volcano 200 years ago. Little is known about other recent eruptions, either at Kiejo or at the other centres (especially at Rungwe or Ngosi volcanoes), although there are numerous Rungwe Volcanic Province ash layers in lakes within a few hundreds of kilometres, indicating frequent explosive eruptions in the province in the last 40 ka. In 2000–2001, a series of tectonic or volcanic earthquakes of moderate magnitude caused damage to villages. Tectonic activity is inferred along the Mbaka Fault (Fig. 9) but no surface rupture has been observed since the 2000–2001 event.

The only geological mapping of the Rungwe Volcanic Province was by Harkin (1960) in the 1950s at 1:250 000. A preliminary re-exploration of this poorly studied volcanic region was conducted using the 90 m SRTM DEM (Fig. 9) and a Landsat TM image. Combined use of these two datasets enhances our capability to understand the geology of the province. The three main eruptive centres are Ngozi volcano, directly south of Mbeya city, Rungwe volcano and the Kiejo volcano. The case of Rungwe volcano is here discussed for illustrative purposes. Rungwe culminates at 2962 m a.s.l. and, like Ngozi, is densely vegetated on its flanks. The Rungwe crater is bordered by a steep semi-circular wall on its NNW to SSE flanks, breached to the SW. Aligned pit craters and scarps, recognizable by their elevation and lack of vegetation, extend along the volcano flanks and are virtually uneroded. From the amphitheatre crater rim, Rungwe is much steeper and with a shorter slope to the NE compared with the SW. These features are interpreted as evidence for a large sector collapse (c. 2–3 km<sup>3</sup>) that produced a debris avalanche. This is corroborated by Harkin's (1960) observations of a striking mound field including perfectly conical 10–20 m diameter hills made up of very poorly sorted, breccia-like material some c. 15–20 km SW from the crater. The RS data spatial resolution, especially that of the 90 m SRTM DEM, does not allow mapping of individual hummocks in itself, but our reinterpretation of Harkin's work using the RS data allowed the mapping of the debris avalanche extent. RS also allows us to establish that several large phonolite–trachyte domes were subsequently emplaced in the Rungwe amphitheatre crater with lava flowing down the breached flank. Lack of vegetation on the most recent flows points to a recent emplacement age, at most of the order of a few centuries. A field campaign is now necessary

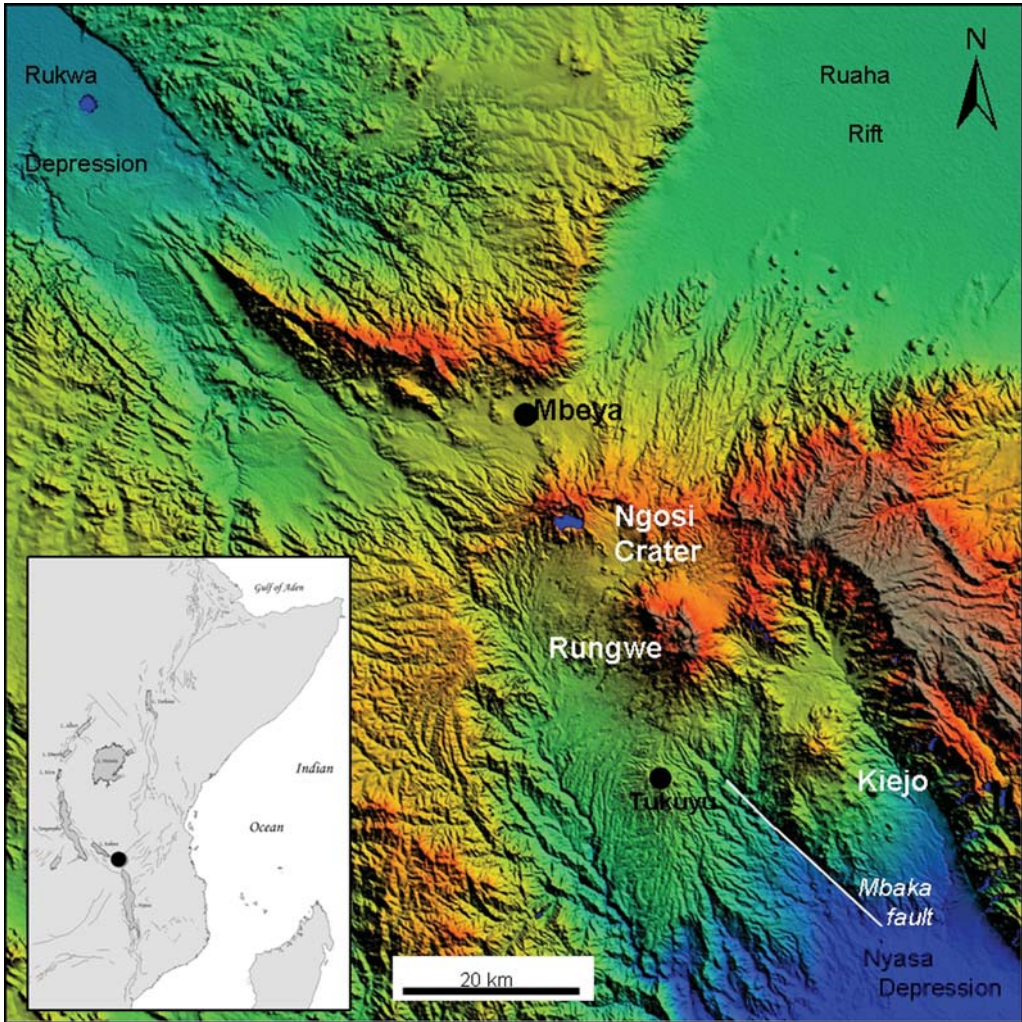


**Fig. 9.** Shaded relief of the 90 m SRTM DEM of Rungwe Volcanic Province, SW Tanzania, with elevation-scaled colour range. Three main phonolite volcanoes and Mbaka Fault are indicated on the image, together with the cities of Mbeya and Tukuyu. The Rift Valley trends NW–SE. Smaller-volume features include phonolite–trachyte domes located in the north and inside Rungwe crater. Inset shows location of the Rungwe Volcanic Province (●) with the East African Rift System.

to validate the hypothesis that this volcano went through a dramatic and hazardous flank collapse event. Sector collapse may have been triggered by the major NW–SE-trending Mbaka Fault extending SW of Kiejo volcano (Fig. 9). As suggested by van Wyk de Vries *et al.* (2003), offset strike-slip faults can trigger volcano-scale collapse. Examination of the Landsat scene and the DEM revealed many small phonolite domes and basaltic cones, which were targeted for ‘ground truth’ field visits. Using recent RS advances, poorly known terrains in the Rungwe Volcanic Province can be rapidly

mapped, at both small and large scales, and hypotheses can be formulated about geohazards in the region.

Now let us consider the challenge of monitoring and studying changes in volcano topography over time, at poorly known and densely vegetated volcanoes, such as Rungwe. Eleven ERS SAR datasets acquired between December 1995 and February 2003 were processed to detect past movements including the 2001 seismic swarm. Dense vegetation causes a rapid loss of coherence in most part of the image and does not allow conventional

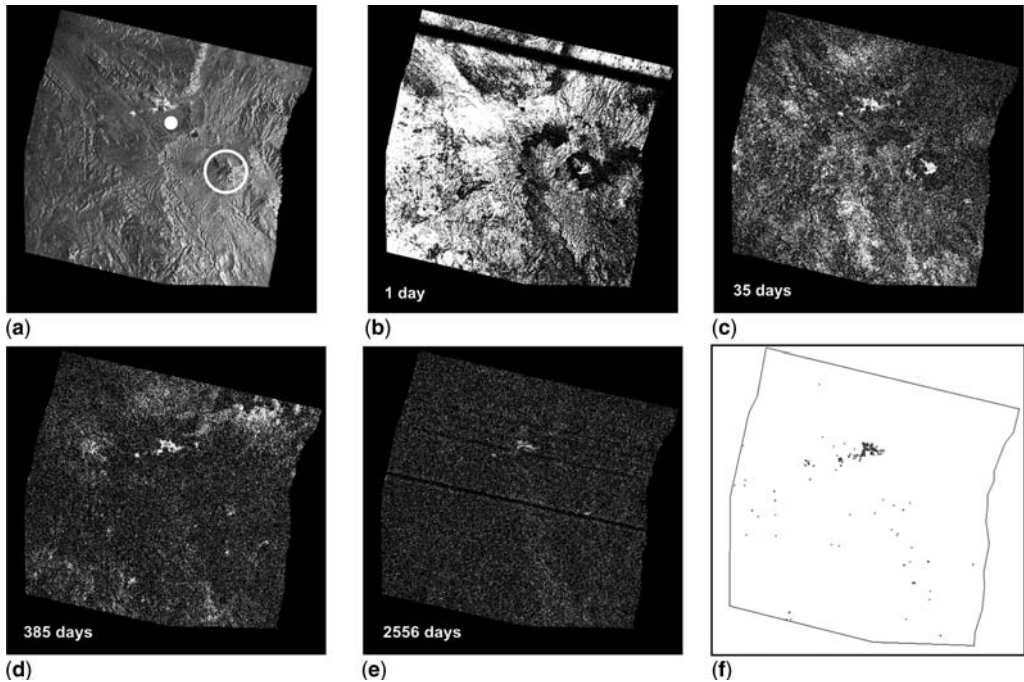


**Fig. 10.** (a) ERS average intensity image (11 looks); white circle and point show locations of Rungwe and of Mbeya, respectively. Bright area in top middle part corresponds to the city of Mbeya. This image was used in the field to locate the PS. (b–e) Maps of coherence above a threshold of 0.35 (white). (b) Coherence after 24 h obtained with the 26–27 September 1997 (dry season) tandem pair. Black patches correspond to densely vegetated areas. The stripe is related to missing lines in one of the two scenes. (c) Coherence after one orbital cycle. High-coherence level remains over urban areas and on bare surface at top of Rungwe (middle-right). (d) Coherence after 1 year. Coherence remains high over Mbeya urban area; top of Rungwe still visible. (e) Coherence after 7 years. Some coherence remains over Mbeya and the top of the Rungwe. (f) Persistent scatterers obtained from the series of coherence maps with a threshold at 0.55. Most of them are located in Mbeya; others correspond to isolated houses with a metal corrugated roof.

differential InSAR to be applied (Fig. 10). With the view of using the persistent scatterers (PS) technique, the data were filtered in such a way that *c.* 600 PS with coherence  $>0.5$  were retained (Table 4). Although the area is densely populated, the only major urban centre is Mbeya, which is also one of the few places where coherence is preserved in the long term. The numerous villages scattered in the image do not provide enough phase stability. Hence, the selected PS distribution is poor and non-uniform (Fig. 10f). A field campaign was specifically dedicated to the PS identification and characterization.

The PS retrieved after the 11 SAR scenes were averaged to (1) produce a multi-look image with a drastic decrease of the speckle and (2) refine image quality. The enhanced geocoded image was then georeferenced with GCPs collected on 1:50 000 scale topographic maps with accuracy better than 2 pixels, i.e. 40 m (RMS). All the PS were then introduced within a hand-held GPS and tracked in the

field. The PS with the highest coherence was found to correspond to a cement factory and nearby warehouses. Other PS correspond mainly to isolated houses or houses with corrugated metal roofs, grouped along two preferential directions (i.e. parallel or perpendicular to the incident radar beam).

For ground deformation monitoring, systematic measurements using the selected PS appear to be noisy and unreliable because of their intrinsic physical properties. The corrugated roofs are made of an assemblage of multiple metal panels fixed on a wooden structure, which itself rests on poor-quality brick walls. In addition to the poor PS density, dilatation–contraction of the metal panels with variations in diurnal insolation or the variable humidity-induced swelling of the wooden structures makes them unsuitable for accurate measurements of crustal deformation.

An alternative way to ‘natural’ PS could be to set up a network of specifically designed corner reflectors in well-selected sites. The advantage is

**Table 4.** Number of pixels with coherence above given thresholds for all interferometric couples derived from 11 ERS SAR scenes

Number of pixels	Coherence threshold					
	0.5	0.55	0.6	0.65	0.7	0.75
	596	227	47	11	2	1

Very few PS points were found after dataset processing. PS number dramatically decreases with the coherence level. The highest coherence target corresponds to a cement factory SW of Mbeya.

the possibility of selecting the location of measurement points, as well as positions of reflectors that can be controlled to validate InSAR measurements. An array of such reflectors can be compared to a GPS array. Such an array of corner reflectors is, however, not easy or cheap to set up. The availability of only sparse reflectors in a large region also poses the problem of correcting for atmospheric water vapour gradients. The attempt to use InSAR to monitor or study ground deformation has helped identify that using the PS or corner reflector approaches does not offer practical solutions. Together with Stevens & Wadge (2004), we stress that the availability of an L-band radar sensor dedicated to ground deformation monitoring might be the only way to enhance the capability of differential InSAR in vegetated terrain. The Rungwe case study illustrates the capabilities of

RS to provide valuable information on the distribution and morphology of eruptive centres, as well as insights into associated hazards, before embarking on field studies. Table 5 summarizes the capabilities and limitations of RS for the study of poorly known volcanoes in developing countries.

### Concluding remarks and perspective

Eighty percent of historically active or dormant, potentially hazardous volcanoes (c. 450 and over 1200 volcanoes, respectively) are located in densely populated developing countries, where populations are also more at risk from natural hazards. The impact of natural disasters there is 20 times higher (as a percentage of GDP per head) than in industrialized countries (World Bank,

**Table 5.** Summary of possibilities and limitations for RS studies of poorly known volcanoes in tropical developing countries

Data Type	Multispectral	Digital Elevation Model	Synthetic Aperture Radar	Differential InSAR
Datasets	Landsat	ASTER – ASTER DEM SPOT – SPOT DEM	InSAR, e.g. SRTM DEM	ERS-1/2, JERS, RADARSAT, ENVISAT (single image)
Derived products	Topomap at 1:25,000 or better			ERS-1/2, JERS, RADARSAT (interferometric couple)
	Volcano-scale morphology			
	Elevation profiles			
	DEMs as baseline for risk models			
	Identification of most faults including large volcano-scale collapse scars			
	Contrasted terrain mapping (e.g. lava flows, pyroclastic flows)			
	Mapping small structures (e.g. domes, cones, vents, pit craters)			
Collection of quantitative morphometric data for hazard modelling*				
Limitations	Cloud cover		Atmospheric effect <sup>†</sup>	Atmospheric effect
		Ground control point quality	Coherence loss in densely vegetated regions <sup>†</sup>	Coherence loss in densely vegetated regions
Challenges			Shadow effect due to angle of viewing – Lack of data in steep craters	Density of permanent coherent scatterers
	Spatial Resolution & Vegetation Cover: Disabling identification of small features (e.g. hummocks in distal zones of debris avalanches)			

\*Lack of theory and experiments useful to invert morphometry for hazard assessment.

†For multiple-pass InSAR techniques.

Hazard Risk Management website 2005). For most of these volcanoes, the detailed geology has not been documented and there may be no or limited geological, geohazard or risk maps. Most of these volcanoes are not currently being monitored. In our experience, sets of aerial photographs may be impossible to obtain, particularly in sub-Saharan Africa. In this vacuum, low-cost satellite data offer the best means of rapidly mapping and monitoring hazardous terrain around volcanoes in developing countries.

We have illustrated that the combined approaches exemplified in this paper allow us to map the full diversity of volcanic terrains at 1:25 000 scale, such as volcanic cones, and pyroclastic or lava flows with contrasting surface textures, as well as structural features, indicating potential volcano-scale instability and geohazards. The combined approaches and individual datasets can be rigorously assessed against each other and are of high quality. Huge volumes of quantitative data can be generated quickly, providing new constraints on volcano shapes, sizes and vent distributions; thus opening up the possibility that these data could be used to mitigate volcanic geohazards.

Landsat and ASTER multispectral archive data, available at low cost, offer great capabilities for exploratory studies of poorly known volcanic terrains and quantitative morphological studies of various volcanic features. ASTER has the advantage over Landsat, in that high-resolution mapping (topography and multispectral) can be derived from the same imagery. However, the cost of near real-time data acquisition continues to limit the use of these data for rapid hazard assessment. ASTER and Landsat ETM+ sensors have also both already reached the end of their designed mission life, and follow-up data acquisition with similar sensors is not yet certain.

All the radar sensors penetrate cloud cover, a major advantage over optical sensors. The fact that only 90 m SRTM data are available worldwide is currently a limitation to mapping hazardous terrains and to mitigating geohazards. Multi-pass InSAR (compared with SRTM single-pass InSAR) looks set to become a powerful tool for deriving 3D topography, facilitating recognition of unstable volcanoes. To recognize flanks prone to instability would, however, require data at higher resolution than provided by current sensors (see Kerle *et al.* 2003). Multi-pass InSAR requires development before it can be effectively used in routine ground deformation monitoring. At present, the main limitations for multi-pass InSAR are changing atmospheric conditions and vegetation cover. As argued by Stevens & Wadge (2004), a dedicated L-band radar might be the way toward operational InSAR monitoring of densely vegetated active volcanoes. In the absence of ground monitoring at most

**Table 6.** Characteristics of recently launched or planned multispectral and radar sensors

Satellite or Sensor	Launch	Bands	Revisit time	Website
RapidEye constellation	2007	5 VNIR; 6.5 m	1 day	<a href="http://www.rapideye.de/">http://www.rapideye.de/</a>
DMC	2002–2005	3 VNIR; 32 m	1 day	<a href="http://www.dmcii.com/">http://www.dmcii.com/</a>
CartoSAT	2005	2 stereo PAN; 2.5 m	5 days	<a href="http://www.isro.org/Cartosat/">http://www.isro.org/Cartosat/</a>
OrbView 5	2007	1 PAN; 0.41 m; 4 VNIR; 1.64 m	< 3 days	<a href="http://www.orbimage.com/">http://www.orbimage.com/</a>
ALOS (PRISM)	2006	1 PAN; 2.5 m	46 days	<a href="http://alos.jaxa.jp/index-e.html">http://alos.jaxa.jp/index-e.html</a>
ALOS (AVNIR-2)	2006	4 VNIR; 10 m	46 days	<a href="http://alos.jaxa.jp/index-e.html">http://alos.jaxa.jp/index-e.html</a>
ALOS (PALSAR)	2006	L-band; 10 m	46 days	<a href="http://alos.jaxa.jp/index-e.html">http://alos.jaxa.jp/index-e.html</a>
ENVISAT (ASAR)	2002	C-band; 25 m	35 days	<a href="http://envisat.esa.int/instruments/asar/">http://envisat.esa.int/instruments/asar/</a>
RADARSAT 2	2006	C-band; 3 m at best	24 days	<a href="http://www.radsat2.info/">http://www.radsat2.info/</a>
TerraSAR	2006	X-band; 1 m at best	11 days	<a href="http://www.terrasar.de/">http://www.terrasar.de/</a>

The list is not exhaustive but presents sensors whose capabilities might be of greatest relevance for volcano hazard assessment. The RapidEye, CartoSat and ALOS (PRISM) sensors offer stereoscopic data. (For more information on these sensors, see the listed website.)



volcanoes in less developed countries, spaceborne monitoring of ground deformation is of crucial importance.

Table 6 summarizes new and planned sensors that should increase RS capabilities to assess hazards at volcanoes. Constellations of small satellites are currently launched to acquire daily multispectral images (e.g. RapidEye and the Disaster Monitoring Constellation, DMC). Sensors will provide data with higher spatial and temporal resolution, but with a limited number of spectral bands. RapidEye, CartoSat and ALOS (PRISM) will provide data with stereoscopic capabilities. High data costs from satellites launched by commercial companies, will, however, limit their usefulness for low-cost geohazard assessment. SAR sensors, with different wavelengths (X, C and L bands; Table 6) should also enhance the possibility of InSAR applications in volcanic terrains. Of special interest is the L-band sensor onboard ALOS, which will ensure enhanced coherence preservation over vegetated terrains.

High spatial resolution topographic data are crucial as a prerequisite to assist geological field work, for morphometric analyses and for volcanic hazard modelling. Satellite remote sensing provides one of the best ways to produce DEMs over extensive volcanic regions, especially in countries where aerial photographs are unavailable.

This paper is dedicated to our colleagues in developing countries who are facing geohazards, some of them in desperate need of acquiring RS monitoring capability. M.K and G.G.J.E are supported by the Belgian NSF (FWO-Vlaanderen) and the 'Fondation Belge de la Vocation'. This effort would not have been possible without the support of UGent colleagues, notably of P. Jacobs and J.-P. Henriët, and without the long-term support of S. Sparks and W. Rose. The Landsat, ASTER and SRTM imagery was obtained from the Global Land Cover Facility website, the Land Processes Distributed Active Archive Center (LPDAAC) website interface, and the Seamless Data Distribution System website.

## References

- ABRAMS, M. & HOOK, S. 2003. *ASTER user handbook version 2*. World Wide Web Address: [http://asterweb.jpl.nasa.gov/documents/aster\\_user\\_guide\\_v2.pdf](http://asterweb.jpl.nasa.gov/documents/aster_user_guide_v2.pdf).
- AirSAR Jet Propulsion Laboratory website 2005. World Wide Web Address: <http://airsar.jpl.nasa.gov/>.
- ALTAIMER, A. & CHRISTOPH, K. 2002. Digital surface model generation from CORONA satellite image. *ISPRS Journal of Photogrammetry and Remote Sensing*, **56**, 221–235.
- AMELUNG, F., JONSSON, S., ZEBKER, H. & SEGALL, P. 2000. Widespread uplift and 'trapdoor' faulting on Galapagos volcanoes observed with radar interferometry. *Nature*, **407**, 993–996.
- ASTERGDS website 2005. World Wide Web Address: <http://www.gds.aster.ersdac.or.jp/>.
- BALDI, P., BONVALOT, S., BRIOLE, P. ET AL. 2002. Validation and comparison of different techniques for the derivation of digital elevation models and volcanic monitoring (Vulcano Island, Italy). *International Journal of Remote Sensing*, **23**, 4783–4800.
- BYRNES, J. M., RAMSEY, M. S. & CROWN, D. A. 2004. Surface unit characterization of the Mauna Ulu flow field, Kilauea Volcano, Hawaii, using integrated field and remote sensing analyses. *Journal of Volcanology and Geothermal Research*, **135**, 169–193.
- CARN, S. A. 1999. Application of Synthetic Aperture Radar (SAR) imagery to volcano mapping in the humid tropics: a case study in East Java, Indonesia. *Bulletin of Volcanology*, **61**, 92–105.
- CHAGARLAMUDI, P. & MOUFTI, M. R. 1991. The utility of Landsat images in delineating volcanic cones in Harrat Kishb, Kingdom of Saudi Arabia. *International Journal of Remote Sensing*, **12**, 1547–1557.
- CONNOR, C. B. & CONWAY, F. M. 2000. Basaltic volcanic cones. In: SIGURDSSON, H., HOUGHTON, B. F., MCNUTT, S. R., RYMER, H. & STIX, J. (eds) *Encyclopedia of Volcanoes*. Academic Press, New York, 331–343.
- COTTON, C. A. 1944. *Volcanoes as Landscape Forms*. Withcombe & Tombs, Christchurch, New Zealand.
- CROWLEY, J. & ZIMBELMAN, D. 1997. Mapping hydrothermally altered rocks on Mount Rainier, Washington, with Airborne Visible Infrared Imaging Spectrometer (AVIRIS) data. *Geology*, **25**, 559–569.
- DAVIS, P. A., BERLIN, G. L. & CHAVEZ, P. S. 1987. Discrimination of altered basaltic rocks in the southwestern United States by analysis of Landsat Thematic Mapper data. *Photogrammetric Engineering and Remote Sensing*, **53**, 51–73.
- DREY, T., POETE, P., THAMM, H.-P., PANNENBECKER, A. & MENZ, G. 2004. Generation of a high resolution DEM with ASTER stereo data for the river Draa catchment in Morocco. IMPETUS Conference Abstracts, Ouarzazae.
- Eurimage website 2005. World Wide Web Address: <http://www.eurimage.com/>.
- FERRETTI, A., PRATI, C. & ROCCA, F. 2001. Permanent scatterers in SAR interferometry. *IEEE Transactions on Geoscience and Remote Sensing*, **39**, 8–20.
- FERRETTI, A., NOVALI, F., BÜRGMANN, R., HILLEY, G. & PRATI, C. 2004. InSAR Permanent Scatterer analysis reveals ups and downs in San Francisco Bay area. *EOS Transactions, American Geophysical Union*, **85**, 317–324.
- FRANCIS, P. W. & BAKER, M. C. W. 1978. Sources of two large volume ignimbrites in the Central Andes: some LANDSAT evidence. *Journal of Volcanology and Geothermal Research*, **4**, 81–87.
- FRANCIS, P. W. & DE SILVA, S. L. 1989. Application of the Landsat Thematic Mapper to the identification of potentially active volcanoes in the Central Andes. *Remote Sensing of Environment*, **28**, 245–255.
- FRANCIS, P. W. & WELLS, G. L. 1988. Landsat Thematic Mapper observations of debris avalanches deposits in the central Andes. *Bulletin of Volcanology*, **50**, 258–278.
- FRANCIS, P. W., WADGE, G. & MOUGINIS MARK, P. J. 1996. Satellite monitoring of volcanoes. In: SCARPA, R. & TILLING, R. I. (eds) *Monitoring and Mitigation of Volcano Hazards*. Springer, Berlin, 257–298.

- GADDIS, L. R. 1992. Lava-flows characterization at Pisgah volcanic field, California, with multiparameter imaging radar. *Geological Society of America Bulletin*, **104**, 695–703.
- GLCF 2005. *Global Land Cover Facilities website*. World Wide Web Address: <http://glcfapp.umiacs.umd.edu/index.shtml>.
- Global Volcanism Program—Smithsonian Institution* 2005. World Wide Web Address: <http://www.volcano.si.edu/>.
- GOOSSENS, R., SCHMIDT, M. & MENZ, G. 2003. High resolution DEM and ortho-photomap generation from TERRA-ASTER data—case study of Morocco. In: BENES, T. (ed.) *Geoinformation for European-wide Integration. Proceedings of the 22nd Symposium of the European Association of Remote Sensing Laboratories*. Millpress, prague, 19–24.
- HARKIN, D. A. 1960. *The Rungwe Volcanics at the Northern End of Lake Nyasa*. Geological Survey of Tanganyika Memoirs, **2**.
- HARRIS, A. J. L., FLYNN, L. P., DEAN, K. ET AL. 2000. Real-time satellite monitoring of volcanic hot spots. In: MOUGINIS-MARK, P. J., CRISP, J. & FINK, J. F. (eds) *Remote Sensing of Active Volcanism*. Geophysical Monograph, American Geophysical Union, **116**, 139–159.
- HARRIS, A. J. L., FLYNN, L. P., MATIOS, O., ROSE, W. I. & CORNEJO, J. 2004. The evolution of an active silicic lava flow field: an ETM + perspective. *Journal of Volcanology and Geothermal Research*, **135**, 147–168.
- HIRANO, A., WELCH, R. & LANG, H. 2003. Mapping from ASTER stereo image data: DEM validation and accuracy assessment. *ISPRS Journal of Photogrammetry and Remote Sensing*, **57**, 356–370.
- HOOPER, A., ZEBKER, H., SEGALL, P. & KAMPES, B. 2004. A new method for measuring deformation on volcanoes and other natural terrains using InSAR persistent scatterers. *Geophysical Research Letters*, **31**, doi: 10.1029/2004GL021737.
- IVERSON, R. M., SCHILLING, S. P. & VALLANCE, J. W. 1998. Objective delineation of lahar-inundation hazard zones. *Geological Society of America Bulletin*, **110**, 972–984.
- KAHLE, A. B., GILLEPSIE, A. R., ABBOTT, E. A., ABRAMS, M. J., WALKER, R. E., HOOVER, G. & LOCKWOOD, J. P. 1988. Relative dating of Hawaiian lava flows using multispectral thermal infrared images: a new tool for geologic mapping of young volcanic terranes. *Journal of Geophysical Research*, **93**, 15239–15251.
- KERLE, N., FROGER, J.-L., OPPENHEIMER, C. & VAN WYK DE VRIES, B. 2003. Remote sensing of the 1998 mudflow at Casita volcano, Nicaragua. *International Journal of Remote Sensing*, **24**, 4791–4816.
- KERVYN, F. 2001. Modelling topography with SAR interferometry: illustrations of favourable and less favourable environment. *Computers & Geosciences*, **27**, 1039–1050.
- KORMUS, W., ALAMUS, R., RUIZ, A. & TALAYA, J. 2004. Assessment of DEM accuracy derived from SPOT 5 High Resolution Stereoscopic imagery. *International Archives of the Photogrammetry, Remote Sensing and Spatial Information Sciences*, **35(B1)**, 445–452.
- LEGELEY-PADOVANI, A., MERING, C., GUILLANDE, R. & HUAMAN, D. 1997. Mapping of lava flows through SPOT images—an example of the Sabancaya volcano (Peru). *International Journal of Remote Sensing*, **18**, 3111–3133.
- LPDAAC 2005. *Land Processes Distributed Active Archive Center, Datapool @ LPDAAC*. World Wide Web Address: <http://edcdaac.usgs.gov/datapool/datapool.asp>.
- LU, Z., FIELDING, E., PATRICK, M. & TRAUTWEIN, C. 2003. Estimating lava volume by precision combination of multiple baseline spaceborne and airborne interferometric synthetic aperture radar: the 1997 eruption of Okmok volcano. *IEEE Transactions on Geoscience and Remote Sensing*, **41**, 1428–1436.
- MASSONNET, D. & FEIGL, K. L. 1995. Discrimination of geophysical phenomena in satellite radar interferograms. *Geophysical Research Letters*, **22**, 1537–1540.
- MCDONALD, R. 1995. CORONA: success for space reconnaissance, a look into the Cold War, and a revolution for intelligence. *Photogrammetric Engineering and Remote Sensing*, **61**, 689–720.
- MCKAY, M. E. & MOUGINIS-MARK, P. J. 1997. The effect of varying acquisition parameters on the interpretation of SIR-C radar data: the Virunga volcanic chain. *Remote Sensing of Environment*, **59**, 321–336.
- MERLE, O. & BORGIA, A. 1996. Scaled experiments of volcanic spreading. *Journal of Geophysical Research*, **101**, 13805–13817.
- MOUGINIS-MARK, P. J., CRISP, J. & FINK, J. (eds) 2000. *Remote Sensing of Active Volcanism*. Geophysical Monograph, American Geophysical Union, **116**.
- NEWHALL, C. G. & PUNONGBAYAN, R. S. (eds) 1996. *Fire and Mud: Eruptions and Lahars of Mount Pinatubo, Philippines*. Philippines Institute of Volcanology and Seismology, Quezon City; University of Washington Press, Seattle.
- OPPENHEIMER, C. 1998. Volcanological application of meteorological satellite data. *International Journal of Remote Sensing*, **19**, 2829–2864.
- PATRICK, M. R., DEHN, J., PAPP, K. R. ET AL. 2003. The 1997 eruption of Okmok Volcano, Alaska: a synthesis of remotely sensed imagery. *Journal of Volcanology and Geothermal Research*, **127**, 87–105.
- PIERI, D. & ABRAMS, M. J. 2004. ASTER watches the world's volcanoes: a new paradigm for volcanological observations from orbit. *Journal of Volcanology and Geothermal Research*, **135**, 13–28.
- PORTER, S. C. 1972. Distribution, morphology and size frequency of cinder cones on Mauna Kea volcano, Hawaii. *Geological Society of America Bulletin*, **83**, 3607–3612.
- RABUS, B., EINEDER, M., ROTH, A. & BAMLER, R. 2003. The Shuttle Radar Topography Mission—A new class of digital elevation models acquired by spaceborne radar. *ISPRS Journal of Photogrammetry and Remote Sensing*, **57**, 241–262.
- RAMSEY, M. & DEAN, J. 2004. Spaceborne observations of the 2000 Bezymianny, Kamchatka eruption: the integration of high-resolution ASTER data into near real-time monitoring using AVHRR. *Journal of Volcanology and Geothermal Research*, **135**, 127–146.
- RAMSEY, M. & FINK, J. H. 1999. Estimating silicic lava vesicularity with thermal remote sensing: a new

- technique for volcanic mapping and monitoring. *Bulletin of Volcanology*, **61**, 32–39.
- RAMSEY, M. S. & FLYNN, L. P. 2004. Strategies, insights and the recent advances in volcanic monitoring and mapping with data from NASA's Earth Observing System. *Journal of Volcanology and Geothermal Research*, **135**, 1–11.
- RIEDEL, C., ERNST, G. G. J. & RILEY, M. 2003. Controls on the growth and geometry of pyroclastic constructs. *Journal of Volcanology and Geothermal Research*, **127**, 121–152.
- ROSE, W. I., BLUTH, G. J. S. & ERNST, G. G. J. 2000. Integrating retrievals of volcanic cloud characteristics from satellite remote sensors: a summary. *Philosophical Transactions of the Royal Society of London, Series A*, **358**, 1585–1606.
- ROWLAND, S. K. 1996. Slope, lava flow volumes, and vent distribution on Volcano Fernandina, Galapagos Islands. *Journal of Geophysical Research*, **101**, 27657–27672.
- ROWLAND, S. K. & GARBEIL, H. 2000. The slopes of oceanic basalt volcanoes. In: MOUGINIS-MARK, P. J., CRISP, J. & FINK, J. (eds) *Remote Sensing of Active Volcanism*. Geophysical Monograph, American Geophysical Union, **116**, 223–247.
- ROWLAND, S. K., SMITH, G. A. & MOUGINIS-MARK, P. J. 1994. Preliminary ERS-1 observations of Alaska and Aleutian volcanoes. *Remote Sensing of Environment*, **48**, 358–369.
- ROWLAND, S. K., MCKAY, M. E., GARBEIL, H. & MOUGINIS-MARK, P. J. 1999. Topographic analysis of Kilauea Volcano, Hawaii, from interferometric airborne radar. *Bulletin of Volcanology*, **61**, 1–14.
- ROWLAND, S. K., HARRIS, A. J. L., WOOSTER, M. J., GARBEIL, H., MOUGINIS-MARK, P. J., AMELUNG, F. & WILSON, L. 2003. Volumetric characteristics of lava flows from interferometric radar and multi-spectral satellite data. *Bulletin of Volcanology*, **65**, 311–330.
- SCHMIDT, M., MENZ, G. & GOOSSENS, R. 2002. Processing techniques for CORONA satellite images in order to generate high-resolution digital elevation models (DEM). In: BÉGNI, G. (ed.) *Observing our Environment from Space: New Solutions for a New Millennium*. Proceeding of the 21st EARSel Symposium. Balkema, Rotterdam, 191–196.
- Seamless Data Distribution System. 2005. World Wide Web Address: <http://seamless.usgs.gov/>.
- SHERIDAN, M. F., HUBBARD, B., CARRASCO-NUNEZ, G. & SIEBE, C. 2004. Pyroclastic flow hazard at Volcan Citlaltépetl. *Natural Hazards*, **33**, 209–221.
- SIMKIN, T. & SIEBERT, L. 1994. *Volcanoes of the World*, 2nd edn. Geosciences Press, Tucson, AZ.
- SRTM mission, JPL website, 2005. World Wide Web Address: <http://www2.jpl.nasa.gov/srtm/>.
- STEVENS, N. F. & WADGE, G. 2004. Towards operational repeat-pass SAR interferometry at active volcanoes. *Natural Hazards*, **33**, 47–76.
- STEVENS, N. F., MANVILLE, V. & HERON, D. W. 2002. The sensitivity of a volcanic flow model to digital elevation model accuracy: experiments with digitised map contours and interferometric SAR at Ruapehu and Taranaki volcanoes, New Zealand. *Journal of Volcanology and Geothermal Research*, **119**, 89–105.
- STEVENS, N. F., GARBEIL, H. & MOUGINIS-MARK, P. J. 2004. NASA EOS Terra ASTER: volcanic topographic mapping and capability. *Remote Sensing of Environment*, **90**, 405–414.
- USGS Earth Explorer website 2005. World Wide Web Address: <http://edcns17.cr.usgs.gov/EarthExplorer/>.
- VAN WYK DE VRIES, B., WOOLLER, L., CECCHI, E. & MURRAY, J. 2003. Spreading volcanoes: The importance of strike-slip faults, EGU General Assembly Conference Abstracts. Nice, Abstract 2480.
- VASSILOPOULOU, S., HURNI, L., DIETRICH, V., BALTSAVIAS, E., PATERAKI, M., LAGIOS, E. & PARCHARIDIS, I. 2002. Orthophoto generation using IKONOS imagery and high-resolution DEM: a case study on volcanic hazard monitoring of Nisyros Island (Greece). *ISPRS Journal of Photogrammetry and Remote Sensing*, **57**, 24–38.
- WADGE, G., FRANCIS, P. W. & RAMIREZ, C. F. 1995. The Socompa collapse and avalanche event. *Journal of Volcanology and Geothermal Research*, **66**, 309–336.
- WIART, P. A. M., OPPENHEIMER, C. & FRANCIS, P. 2000. Eruptive history of Dubbi volcano, northeast Afar (Eritrea), revealed by optical and SAR image interpretation. *International Journal of Remote Sensing*, **21**, 911–936.
- WILLIAMS, D. 2003. *Landsat 7, Science data user handbook*. Landsat Project Science Office. World Wide Web Address: [http://ftpwww.gsfc.nasa.gov/IAS/handbook/handbook\\_toc.html](http://ftpwww.gsfc.nasa.gov/IAS/handbook/handbook_toc.html).
- WOLFE, E. W., WISE, W. S. & DALRYMPLE, G. B. 1997. The Geology and Petrology of Mauna Kea, a Study of Postshield Volcano. *US Geological Survey, Professional Papers*, **1557**.
- WOOD, C. A. 1980a. Morphometric evolution of cinder cones. *Journal of Volcanology and Geothermal Research*, **7**, 387–413.
- WOOD, C. A. 1980b. Morphometric analysis of cinder cone degradation. *Journal of Volcanology and Geothermal Research*, **8**, 137–160.
- World Bank, Hazard Risk Management website 2005. World Wide Web Address: [www.worldbank.org/hazards/](http://www.worldbank.org/hazards/).
- WRIGHT, R., FLYNN, L. P., GARBEIL, H., HARRIS, A. J. L. & PILGER, E. 2004. MODVOLC: near-real time thermal monitoring of global volcanism. *Journal of Volcanology and Geothermal Research*, **135**, 29–49.
- X-SAR SRTM website 2005. World Wide Web Address: [http://www.dlr.de/SRTM/SRTM\\_en.html](http://www.dlr.de/SRTM/SRTM_en.html).
- ZEBKER, H. & VILLASENOR, J. 1992. Decorrelation in interferometric radar echoes. *IEEE Transactions on Geoscience and Remote Sensing*, **30**, 950–959.
- ZEBKER, H. A., WERNER, C. L., ROSEN, P. A. & HENSLEY, S. 1994. Accuracy of topographic maps derived from ERS-1 interferometric radar. *IEEE Transactions on Geoscience and Remote Sensing*, **32**, 823–836.
- ZEBKER, H. A., AMELUNG, F. & JONSSON, S. 2000. Remote sensing of volcano surface and internal processes using radar interferometry. In: MOUGINIS-MARK, P. J., CRISP, J. & FINK, J. (eds) *Remote Sensing of Active Volcanism*. Geophysical Monograph, American Geophysical Union, **116**, 179–205.